

A μ -opioid receptor modulator that works cooperatively with naloxone

<https://doi.org/10.1038/s41586-024-07587-7>

Received: 6 July 2023

Accepted: 21 May 2024

Published online: 3 July 2024

 Check for updates

Evan S. O'Brien¹, Vipin Ashok Rangari², Amal El Daibani², Shainnel O. Eans³, Haylee R. Hammond³, Elizabeth White¹, Haoqing Wang¹, Yuki Shiimura^{1,4}, Kaavya Krishna Kumar¹, Qianru Jiang², Kevin Appourchaux², Weijiao Huang¹, Chensong Zhang⁵, Brandon J. Kennedy⁶, Jesper M. Mathiesen⁷, Tao Che², Jay P. McLaughlin³✉, Susruta Majumdar²✉ & Brian K. Kobilka¹✉

The μ -opioid receptor (μ OR) is a well-established target for analgesia¹, yet conventional opioid receptor agonists cause serious adverse effects, notably addiction and respiratory depression. These factors have contributed to the current opioid overdose epidemic driven by fentanyl², a highly potent synthetic opioid. μ OR negative allosteric modulators (NAMs) may serve as useful tools in preventing opioid overdose deaths, but promising chemical scaffolds remain elusive. Here we screened a large DNA-encoded chemical library against inactive μ OR, counter-screening with active, G-protein and agonist-bound receptor to 'steer' hits towards conformationally selective modulators. We discovered a NAM compound with high and selective enrichment to inactive μ OR that enhances the affinity of the key opioid overdose reversal molecule, naloxone. The NAM works cooperatively with naloxone to potently block opioid agonist signalling. Using cryogenic electron microscopy, we demonstrate that the NAM accomplishes this effect by binding a site on the extracellular vestibule in direct contact with naloxone while stabilizing a distinct inactive conformation of the extracellular portions of the second and seventh transmembrane helices. The NAM alters orthosteric ligand kinetics in therapeutically desirable ways and works cooperatively with low doses of naloxone to effectively inhibit various morphine-induced and fentanyl-induced behavioural effects *in vivo* while minimizing withdrawal behaviours. Our results provide detailed structural insights into the mechanism of negative allosteric modulation of the μ OR and demonstrate how this can be exploited *in vivo*.

Traditional opioid compounds extracted from *Papaver somniferum*, including morphine, have been used both recreationally and as potent pain relief molecules for millennia. Related semi-synthetic derivatives such as oxycodone have been extensively prescribed clinically as analgesics. Opioids represent best-in-class treatments for acute pain management¹, yet have also been overused as long-term analgesic treatments. Their high potential for addiction and abuse, in conjunction with their severe respiratory depression effects, have fuelled the current opioid overdose epidemic^{1,3,4}. Increasing numbers of patients are becoming addicted to over-prescribed opioids, and fully synthetic (and more potent) opioid agonists such as fentanyl have been exploited as inexpensive additives to recreationally used opioid mixtures^{2,5}. Naloxone (Narcan) is the most common and effective treatment for opioid overdoses; however, larger and repeated doses are needed in response to overdoses from more potent and long-lasting opioids such as fentanyl^{5,6}.

All these molecules share a similar mode of action as orthosteric agonists of the μ OR, albeit with different affinities for the receptor and extents of intracellular signalling (efficacies). Agonists and antagonists of the μ OR bind at an overlapping orthosteric site in the extracellular vestibule of the receptor and share a set of key interactions with endogenous opioid signalling peptides, namely the enkephalins, endorphins and endomorphins^{7–10}. Given the limitations of the current range of orthosteric opioid molecules, as well as the severity of the current opioid overdose epidemic, new classes of μ OR-modulating compounds with distinct mechanisms of action are desirable and have emerged as priorities of the National Institute of Drug Abuse¹¹.

Rather than further explore agonism at the traditional orthosteric site, modulation of receptor activity through binding of molecules at alternative sites on the receptor (allosteric sites) potentially provides a series of advantages. Distinct signalling bias and functional selectivity *in vivo* can be achieved by extending orthosteric molecules into

¹Department of Molecular and Cellular Physiology, Stanford University School of Medicine, Stanford, CA, USA. ²Center for Clinical Pharmacology, University of Health Sciences and Pharmacy at St Louis and Washington University School of Medicine, St Louis, MO, USA. ³Department of Pharmacodynamics, University of Florida, Gainesville, FL, USA. ⁴Division of Molecular Genetics, Institute of Life Science, Kurume University, Fukuoka, Japan. ⁵Division of CryoEM and Bioimaging, SSRL, SLAC National Acceleration Laboratory, Menlo Park, CA, USA. ⁶Lotus Separations, Princeton University, Princeton, NJ, USA. ⁷Department of Drug Design and Pharmacology, University of Copenhagen, Copenhagen, Denmark. ✉e-mail: jpmclaughlin@ufl.edu; susrutam@wustl.edu; kobilka@stanford.edu

allosteric pockets¹². Allosteric modulators may act more specifically through the μ OR (rather than its κ -opioid receptor (κ OR) and δ -opioid receptor (δ OR) counterparts) owing to decreased evolutionary similarity outside the conserved opioid receptor orthosteric pocket. Allosteric modulators can sometimes display ‘probe dependence’, preferentially modulating the activity of one orthosteric molecule over others¹³. For instance, NAMs that are more effective against exogenous than endogenous agonists would be desirable. Certain small molecules, including cannabinoids¹⁴ and the selective κ OR agonist salvinorin A¹⁵, have been identified as NAMs of the μ OR, although their potencies for their selective targets (cannabinoid receptor 1 (CB1) and κ OR) are higher than those observed against the μ OR (high micromolar concentrations), which suggests that they are highly unlikely to display selective μ OR–NAM activity *in vivo*. Selective, potent NAMs for the μ OR have remained elusive.

We set out to identify such compounds through a directed screen of a large DNA-encoded chemical library (DEL) composed of a series of small fragments covalently linked together in a combinatorial manner (Fig. 1a). The fragments are all conjugated to a DNA barcode sequence that identifies the molecule to which it is linked. Owing to this combinatorial nature, DELs can be composed of billions or even trillions of individual components covering large areas of chemical space^{16–18}. This approach has been used to identify positive and negative allosteric modulators for the β_2 -adrenergic receptor^{19–22}. However, previous GPCR DEL selections have relied on a single receptor condition (for example, agonist-bound receptor¹⁹), which requires the synthesis of large numbers of compounds to identify those that bind the target and have the desired biological activity. Our steered screening approach (Fig. 1a), centred around counter-screening inactive, naloxone-bound receptor against active, G_i -bound μ OR, resulted in the discovery of a potent μ OR NAM from the synthesis of a single compound. Using cryogenic electron microscopy (cryo-EM), we demonstrate that this molecule caps the orthosteric antagonist naloxone in the orthosteric pocket and inhibits receptor activity by stabilizing a distinct inactive conformation of the extracellular vestibule. Potent inhibition of receptor activity only occurs in the presence of the cooperative binding of naloxone, consistent with the structure. This activity translates to *in vivo* mouse models, in which the NAM works cooperatively to boost the ability of low doses of naloxone to reverse opioid-induced effects, including those from fentanyl, while minimizing withdrawal symptoms.

Targeted DEL screen for GPCR NAMs

To discover NAMs that inhibit activation of the receptor, we selected for DEL components that bind specifically to μ ORs saturated with naloxone (condition 1, Fig. 1a). To select against compounds that bind in a non-conformationally sensitive manner (silent allosteric modulators) or that have some binding propensity to the active conformation of the receptor, we included μ OR bound to agonist (met-enkephalin) and G_i as a fully active anti-target (condition 2, Fig. 1a). Finally, no target control (condition 3, Fig. 1a) eliminates molecules that bind nonspecifically to the beads used to immobilize receptors. Molecules that bind specifically to condition 1 and minimally to the others are likely to be μ OR NAMs.

After several rounds of binding the DEL to all conditions and washing away unbound components, the enriched components were subjected to next-generation sequencing. Relative enrichment scores were then calculated based on the number of sequence reads for each condition (Fig. 1b). There were several families of enriched compounds in all conditions, an example of which is highlighted in Fig. 1b, with individual family members sharing one or two fragments in common (Extended Data Table 1). All members were specifically enriched in the inactive form of μ OR. We selected the best-enriched compound (10105-368-30-605, called **368** hereafter; calculated properties are presented in Extended Data Fig. 1a) without detectable binding to anti-targets for

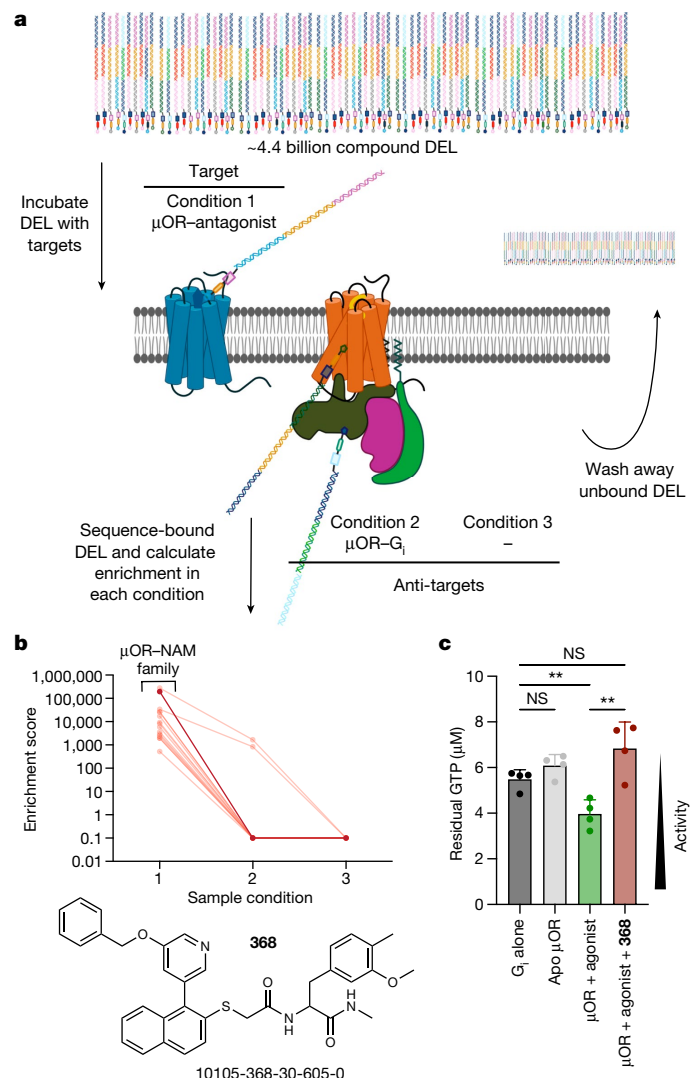


Fig. 1 | DEL screen for new μ OR allosteric modulators. **a**, Schematic detailing the DEL selection scheme including target (condition 1, inactive μ OR–naloxone), anti-target (condition 2, active μ OR– G_i) and no target control (condition 3, –). **b**, Enrichment scores for **368** (solid) and related family members (semi-transparent) across the three sample conditions. The chemical structure for **368** is displayed below. **c**, GTP turnover assay used to initially assess the activity of the NAM. G_i alone has intrinsic GTPase activity (dark grey) that is not significantly affected by the presence of apo μ OR (light grey) ($P = 0.114$), but is enhanced when the receptor is bound to the full agonist peptide met-enkephalin (green) ($P = 0.007$). The NAM (red) significantly inhibits agonist-induced turnover ($P = 0.005$) back to levels that are indistinguishable from G_i alone ($P = 0.071$). Final concentrations of μ OR and G_i were $0.5 \mu\text{M}$, and met-enkephalin and **368** were present at $20 \mu\text{M}$. Data are represented as the mean \pm s.d. of $n = 4$ individual experiments. P values were calculated using unpaired t -test (two-tailed) and are denoted as follows: NS, not significant ($P > 0.05$), * $P \leq 0.05$, ** $P \leq 0.01$, *** $P \leq 0.001$ and **** $P \leq 0.0001$. Schematic in **a** was created using BioRender (<https://biorender.com>).

further characterization. We first tested for activity using an *in vitro* GTP-turnover assay^{23,24} in which we assessed the ability of **368** to dampen agonist-dependent GTP depletion. **368** significantly inhibited met-enkephalin-induced μ OR activation of G_i (Fig. 1c). The observed inhibition of GTP turnover in the presence of the NAM only occurred in the presence of receptor and G_i (Extended Data Fig. 1b). Given the large (and conformationally selective) enrichment and observed activity of **368** as a μ OR inhibitor, we were interested in extensively characterizing its mechanism of action.

Pharmacology of 368

Using the GTP-depletion assay, we first showed that **368** inhibits μ OR and met-enkephalin-induced activation of G_i , with an observed potency in the single-digit micromolar range (Fig. 2a). However, the concentration of the receptor was on the same scale, which made quantitative evaluation of potencies difficult. The effect saturated at around 10 μ M **368**, nearly eliminating receptor-induced GTP turnover (Fig. 2a). To assess the potency of **368** more quantitatively, we observed its effect on 3 H-naloxone binding to μ OR-expressing membranes. Consistent with its selective enrichment to inactive, naloxone-bound receptor and its inhibition of μ OR-induced inhibition of G_i signalling, titrating **368** resulted in increased binding of 3 H-naloxone, with an EC_{50} of 133 nM (Fig. 2b). This increase in binding was the result of an around 2.6-fold increase in 3 H-naloxone affinity in the presence of 2 μ M **368** (Extended Data Fig. 1c).

Introduction of **368** resulted in inhibition of receptor-catalysed GTP turnover in the absence of an orthosteric ligand (Fig. 2c), which designated the molecule as an inverse agonist NAM for the μ OR. It also inhibited additional turnover caused by the weak partial agonist and neutral antagonist naloxone, as well that from the full agonist H-Tyr-D-Ala-Gly-N(Me)Phe-Gly-OH (DAMGO) (Fig. 2c). μ OR has minimal basal signalling, and additional signalling from naloxone was weak. It remains unclear whether inhibition of these low levels of signalling is physiologically relevant. Binding of **368** inhibited μ OR-induced signalling when bound to a variety of orthosteric agonists (Extended Data Fig. 1d), though excess (that is, high double-digit micromolar) concentrations of NAM were present.

We next conducted a series of in-cell TRUPATH²⁵ assays to test the effect of **368** on G-protein activation in cells. We tested several orthosteric agonists (morphine, fentanyl and met-enkephalin) and all $G\alpha$ -protein family members through which μ OR signals (G_{i1} , G_{i2} , G_{i3} , G_{oA} , G_{oB} and G_z). The observed potency in the TRUPATH assays for all three ligands was decreased by more than tenfold in the presence of **368** (Extended Data Fig. 1e–g and Extended Data Table 2), with all $G_{i/o}$ subtypes inhibited in potencies at nearly equal levels (Extended Data Fig. 1h). This result indicated there was no obvious biased negative allosterism of **368** across $G_{i/o}$ family members. Agonist stimulation of receptors predominantly coupled to $G_{i/o}$ family G proteins resulted in decreased cAMP levels. We next tested whether the observed **368** inhibition of agonist potency for dissociating G-proteins translates to inhibition of agonist-induced decreases in cAMP levels. The titration of increasing concentrations of **368** at EC_{80} levels of orthosteric agonist resulted in a dose-dependent increase in cAMP levels (Extended Data Fig. 1i), although the observed potency for agonist inhibition was low (around double-digit micromolar concentrations).

Higher concentrations of **368** were needed to observe inhibition of agonist-induced μ OR signalling both biochemically (Fig. 2a) and in cell-based assays (Extended Data Fig. 1e–i) than would be expected from its potency in enhancing naloxone affinity (Fig. 2b). To resolve these discrepancies, we next tested the hypothesis that **368** requires the presence of orthosteric naloxone to potently inhibit receptor turnover (that is, it is a probe-dependent NAM for naloxone). To that end, we conducted a TRUPATH²⁵ assay in antagonist mode for μ OR-expressing cells, titrating in naloxone to observe inhibition of G-protein heterotrimer dissociation using bioluminescence resonance energy transfer (BRET). The observed potency of naloxone for inhibiting agonist-induced signalling was enhanced by 7.6-fold in the presence of **368** (Fig. 2d). This cooperation with naloxone binding, observed biochemically and in cells, is also a direct demonstration of the allosteric mechanism of action of the compound, at least with respect to this particular antagonist. Consistently, single-digit micromolar concentrations of **368** alone were unable to inhibit met-enkephalin or morphine agonism at EC_{80} concentrations (Extended Data Fig. 1i) in cAMP assays. However, the same concentrations resulted in significant enhancements in the

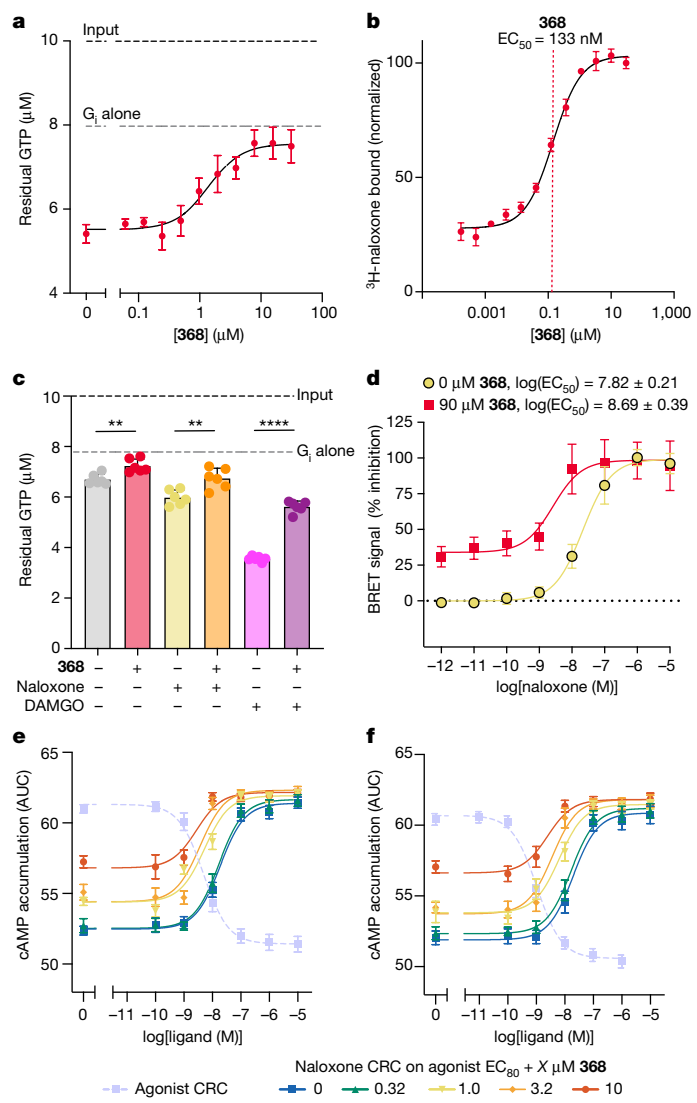


Fig. 2 | 368 inhibits turnover together with naloxone. **a**, Introduction of increasing concentrations of **368** to the GTP turnover assay results in nearly full inhibition of excess (20 μ M) met-enkephalin-bound receptor-mediated turnover with a potency in the single-digit micromolar range. Data are represented as the mean \pm s.d. with $n = 6$ individual experiments. **b**, Increasing concentrations of **368** result in an increase in 3 H-naloxone binding to the receptor with an observed EC_{50} of 133 nM (95% confidence interval (CI) of 112–159 nM) (dashed red line). Data are represented as the mean \pm s.d. with $n = 4$ individual experiments. **c**, GTP turnover assay with excess concentrations of **368**, antagonist naloxone or full agonist DAMGO. **368** significantly inhibits basal signalling (grey versus red, $P = 0.0029$), the weak partial activity of naloxone (yellow versus orange, $P = 0.0040$) and the full activity of DAMGO (pink versus purple, $P < 0.0001$). Final concentrations of all ligands were 20 μ M, with G_i at 0.5 μ M and μ OR at 1 μ M. Data are represented as the mean \pm s.d. with $n = 6$ individual experiments. **d**, Reversal of DAMGO-induced G_i activation by the μ OR through the titration of naloxone in the absence (yellow) or presence (red) of **368**. Data are represented as the mean \pm s.d. with $n = 12$ individual experiments. **e,f**, cAMP levels decrease after increasing concentrations of morphine (**e**) or fentanyl (**f**) (light blue dashed curves). Naloxone concentration-response curves (CRCs) (solid curves) at EC_{80} concentrations of agonist result in reversal of cAMP depletion. Increasing concentrations of **368** result in a left-shift in naloxone potencies, with clear effects observed at single-digit micromolar concentrations (light and dark green curves). Data are represented as the mean \pm s.e.m. with $n = 6$ individual experiments. P values were calculated using unpaired t -test (two-tailed) and are denoted as follows: NS ($P > 0.05$), * $P \leq 0.05$, ** $P \leq 0.01$, *** $P \leq 0.001$ and **** $P \leq 0.0001$.

observed potency of naloxone to inhibit morphine (Fig. 2e) and, importantly, fentanyl (Fig. 2f).

In summary, biochemical and in-cell studies suggest that **368** acts as an inhibitor of μ OR-stimulated G-protein activation by several distinct orthosteric agonists. The enhancement in the affinity of orthosteric antagonist naloxone in the presence of **368** (with an EC_{50} of about 133 nM) suggests that the compound is allosteric with respect to naloxone. Finally, **368** acts more potently to inhibit various agonist signalling through the μ OR in in-cell assays in the presence of naloxone (Fig. 2e,f) than on its own (Extended Data Fig. 1e–i), which suggests that it is a probe-dependent NAM with naloxone.

Structure of **368**-bound μ OR

No potent, specific NAMs exist for the μ OR, although some ligands for other receptors (including CBL) can act as weak NAMs at μ OR^{14,26}. As **368** seems to have these desirable properties, we performed a detailed structural characterization of its mechanism of action. To that end, we bound Nb6, an inactive κ OR-specific nanobody^{27,28}, to a μ OR- κ OR(ICL3) chimera in the presence of naloxone and **368**, following established methodology for the determination of structures of inactive GPCRs²⁹ (Extended Data Fig. 2a). The complex was purified on Flag resin (Extended Data Fig. 2a) and subjected to cryo-EM imaging (Extended Data Fig. 2b). A final density map at 3.26 Å nominal resolution (Extended Data Fig. 2b and Extended Data Table 3) was then used to unambiguously place naloxone in the orthosteric pocket (Fig. 3a and Extended Data Fig. 2b). We also observed density adjacent to naloxone (Fig. 3a), not previously observed in other inactive μ OR structures^{29,30}. Although the initial hit for **368** was a racemic mixture due to a single stereocentre, DEL enrichment data suggested better binding for the S-isomer (Extended Data Fig. 3a). We designed synthetic strategies to produce individual enantiomers of **368** (described in detail in the Methods, schemes 1–3). A multi-gram scale synthesis of (S)-**368** and (\pm)-**368** was also developed. We used (\pm)-**368** to establish a chiral chromatography method for separation of individual enantiomers (Extended Data Fig. 3b). With this method, we next showed that our separately synthesized individual enantiomers are indeed highly enantiomerically pure (98% and 99% for (S)-**368** and (R)-**368**, respectively) (Extended Data Fig. 3c,d). Using this enantiomerically pure material (confirmed by chiral supercritical fluid chromatography; Extended Data Fig. 3b–d), we demonstrated that the S-isomer was the active species by both radio-ligand binding (Extended Data Fig. 3e) and GTP depletion (Extended Data Fig. 3f) assays. Thus, (S)-**368** was placed and docked into the final density map. The resulting structure without Nb6 was also simulated for three independent 200 ns simulations with root mean square deviation (r.m.s.d.) values for the protein backbone, naloxone and (S)-**368** remaining near or under 2 Å (Extended Data Fig. 3g–j), consistent with stable poses for both molecules. To further support the proposed NAM pose, we demonstrated that simulations initiated from a less optimal (although still plausible) pose for the compound immediately and consistently departed from the starting pose, resulting in high r.m.s.d. values (>3–5 Å) from the input structure (Extended Data Fig. 3g–j).

Finally, we disrupted specific interactions within the (S)-**368** binding site by mutating hydrogen bonding partners to nonpolar residues or by disrupting packing interactions with the NAM. Introducing steric clash by mutating an alanine involved in hydrophobic packing with (S)-**368** to leucine (A323L) decreased the observed affinity of **368** for enhancing 3 H-naloxone binding (Extended Data Fig. 4a). Moreover, the mutation substantially reduced the extent of the observed improvement in 3 H-naloxone affinity (Extended Data Fig. 4a) and reduced NAM activity against both morphine and fentanyl in the in-cell TRUPATH assay (Extended Data Fig. 4b–d). Introducing a bulky aromatic ring on the other side of the phenyl ring in (S)-**368** (I71W) also decreased the affinity of **368** by radioligand binding (Extended Data Fig. 4a). Inserting a charge into a hydrophobic interaction on the opposite end of the

(S)-**368**-binding site (I144E) eliminated NAM activity against morphine and fentanyl in the TRUPATH assay (Extended Data Fig. 4b–d). Finally, elimination of a key hydrogen bond between H319 and (S)-**368** by mutating it to leucine (H319L) dampened NAM activity against morphine (Extended Data Fig. 4b,c), but the mutation alone significantly altered fentanyl signalling (Extended Data Fig. 4d). These results highlight the proximity of NAM and orthosteric agonist binding sites. All mutations tested in TRUPATH assays were expressed at >50% of the levels seen for the wild-type receptor (Extended Data Fig. 4b). There was additional well-resolved density further removed from the orthosteric and allosteric sites towards the extracellular space. This result could be due to buffer or lipid components, alternative **368** conformations or enantiomers, or representative of a structured amino-terminal conformation of the receptor as previously reported³¹.

The orthosteric naloxone binds in a similar pocket to the covalent antagonist β -FNA³⁰ (Extended Data Fig. 5a, interacting residues shown in Fig. 3b, right). (S)-**368** binds in the extracellular vestibule region in direct proximity to naloxone (Fig. 3b), forming a stabilizing hydrogen bond with a hydroxyl group in naloxone not present in morphine (Fig. 3b, bottom). Physical contact with naloxone, as well as a slight restriction in access to extracellular solution (Extended Data Fig. 5a), may explain its enhanced affinity in the presence of **368** (Fig. 2b). Both orthosteric naloxone (Fig. 3c, yellow) and **368** (Fig. 3c, red) are well-defined within the cryo-EM density map. We were interested in whether **368** binding also directly affects ligand kinetics. 3 H-naloxone exhibited a relatively short half-life on purified μ OR of 2.8 min (Fig. 3d, yellow). In the presence of **368**, the observed 3 H-naloxone binding was increased, consistent with previous results demonstrating the NAM enhancement of naloxone affinity for the receptor (Fig. 2b and Extended Data Fig. 1c). Furthermore, no observed decrease in 3 H-naloxone binding occurred over the course of the experiment (about 30 min; Fig. 3d, red), which demonstrates that this enhanced affinity is due, at least in part, to a decreased off-rate from the receptor, consistent with structural predictions (Extended Data Fig. 5a). Overlay of various active, agonist-bound structures with (S)-**368**-bound receptor indicated little direct clash with small-molecule agonists (Extended Data Fig. 5b, top) and extensive clash with peptide agonists (Extended Data Fig. 5b, bottom). (S)-**368** may then act more like a competitive antagonist for endogenous opioids and a NAM for small-molecule opioids. This being said, **368** binding is probably incompatible with the active conformations of the extracellular regions of the receptor stabilized by all of these agonists. That is, in the absence of stabilizing contacts and inactive receptor conformations induced by naloxone binding, **368** potency remains low regardless of the orthosteric ligand.

We next tested the ability of **368** to inhibit signalling by other opioid receptor types (μ OR, δ OR and κ OR) using the TRUPATH assay. Increasing concentrations of **368** (up to 30 μ M) resulted in a 3.7-fold right-shift in DAMGO potency at the μ OR (Extended Data Fig. 5c), consistent with its activity described above. The NAM also caused a right-shift in DPDPE potency at δ OR, although to a lesser extent (2.9-fold) (Extended Data Fig. 5d). No effect was observed for κ OR activation by U50,488 (Extended Data Fig. 5e). Sequence alignment of key regions of the receptor interacting with **368** showed that there is extensive conservation in most areas of the binding site (Extended Data Fig. 5f) but with some important exceptions, including an area at the beginning of seventh transmembrane 7 (TM7) helix including several aromatic residues (W318^{7,35} and H319^{7,36}; superscripts indicate Ballesteros-Weinstein numbering used for GPCRs) predicted to make key interactions with **368** in the μ OR.

368 binds to a distinct inactive conformation of μ OR

368 does not act solely through favourable contacts with bound orthosteric naloxone (Fig. 3b, bottom). It also makes a series of inactive-state-specific interactions across the entire vestibule, ranging

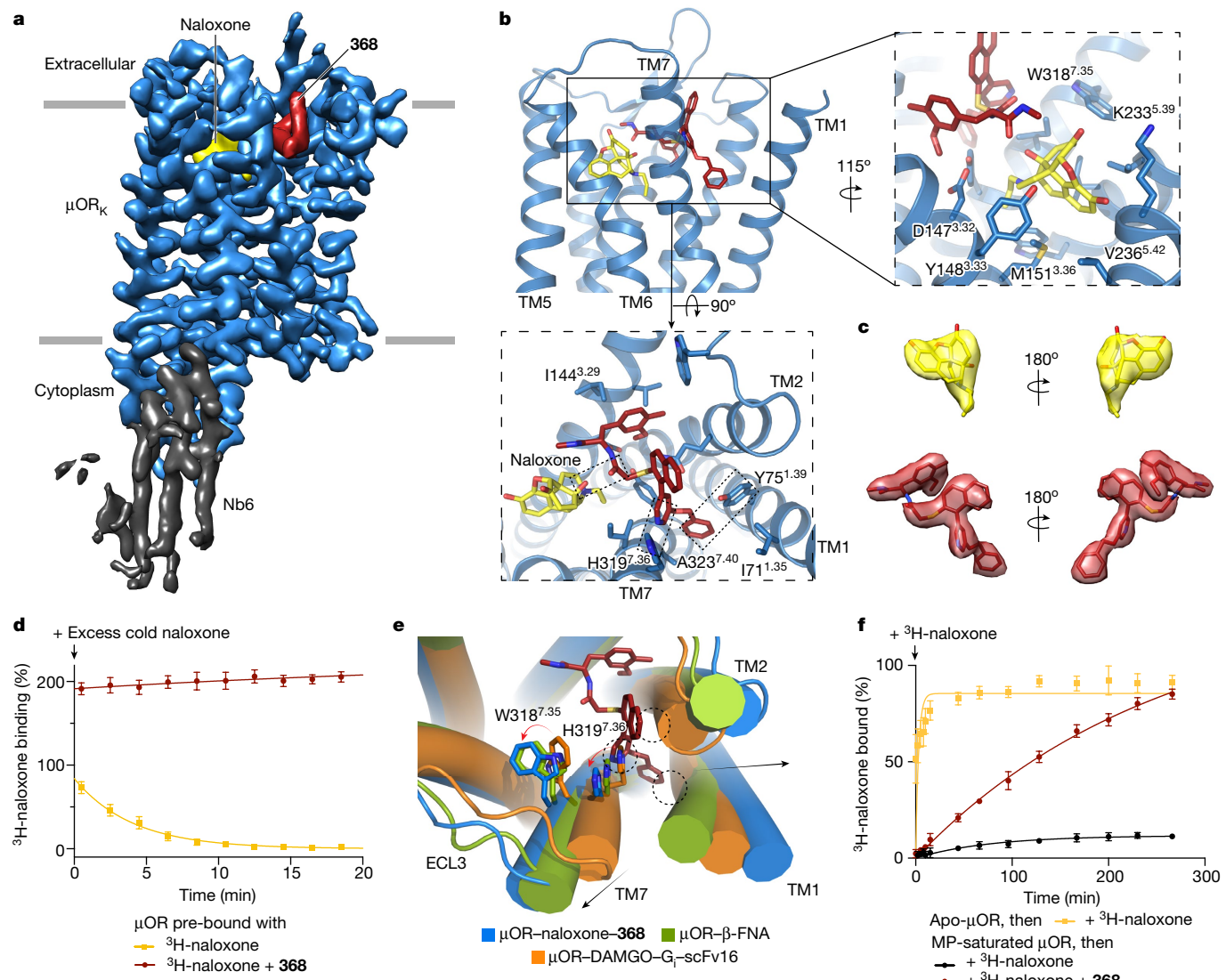


Fig. 3 | Structural mechanism of 368 NAM activity. **a**, Cryo-EM density map of naloxone, 368 and Nb6-bound μ OR- κ OR (μ OR κ) coloured by subunit. Map contour level 0.93 in Chimera. **b**, Naloxone (right) forms a series of inactive-state interactions with μ OR, although it also directly interacts with 368. 368 forms a series of interactions across the extracellular vestibule of the receptor (bottom), ranging from hydrophobic interactions with I144^{3.29} and V143^{3.28} in TM3 to hydrogen bonding with H319^{7.36} in TM7 and π - π interactions with Y75^{1.39} in TM1. Key interactions are shown in dashed boxes. **c**, Cryo-EM density maps of naloxone (yellow) and 368 (red). Map contour level 0.93 in Chimera. **d**, The off-rate of 3 H-naloxone from μ OR was measured in the absence (yellow) or presence (red) of 368. Data are displayed as the mean per cent binding \pm s.d. of $n = 4$ individual experiments, normalized to nonspecific binding (0%) and values in the absence of introduction of cold naloxone (100%).

from the orthosteric site to residues in TM1, TM2 and TM7. A notable feature of the 368-bound μ OR is the extreme outward movement of TM1, a conformation forced by the ‘intercalation’ of the terminal benzene moiety in the NAM between TM1 and TM7 (Fig. 3e) driven by π - π interactions of 368 with Y75^{1.39} (Fig. 3b, bottom). However, this farther outward vestibule conformation does not seem to be correlated with the receptor activation state. The naphthalene ring in 368 is in a position that would result in extensive steric clash with the extracellular half of TM2 in the DAMGO-G_i-bound active state³² of the receptor (Fig. 3e). NAM binding is also incompatible with the TM2 conformation observed in a previously published inactive, β -FNA-bound

structure³⁰ (Fig. 3e), resulting in a further outward movement of the helix compared with previous active and inactive conformations of TM2. The nitrogen in the pyridine ring of 368 is hydrogen bonded with H319^{7.36} in TM7, an interaction that can only be formed in the inactive conformation of TM7, as H319^{7.36} in the active DAMGO-bound state of the receptor is in direct clash with the NAM (Fig. 3e). Outward movement of the extracellular region of TM7 results in stabilization of the W318^{7.35} side chain and the entire third extracellular loop (ECL3) in an inactive conformation (Fig. 3e). These TM7 interactions with the NAM force the extracellular half of TM7 into an even farther outward state compared with previous structures, potentially consistent with the

structure³⁰ (Fig. 3e), resulting in a further outward movement of the helix compared with previous active and inactive conformations of TM2. The nitrogen in the pyridine ring of 368 is hydrogen bonded with H319^{7.36} in TM7, an interaction that can only be formed in the inactive conformation of TM7, as H319^{7.36} in the active DAMGO-bound state of the receptor is in direct clash with the NAM (Fig. 3e). Outward movement of the extracellular region of TM7 results in stabilization of the W318^{7.35} side chain and the entire third extracellular loop (ECL3) in an inactive conformation (Fig. 3e). These TM7 interactions with the NAM force the extracellular half of TM7 into an even farther outward state compared with previous structures, potentially consistent with the

observed biochemical activity of **368** as a further inhibitor of naloxone partial agonism (Fig. 2c).

Given this series of inactive-state-specific interactions at residues allosteric to the conventional opioid-binding site, we speculated that **368** may modulate off-rates of opioid agonists. We saturated purified μ OR with the potent partial agonist mitragynine pseudoindoxyl (MP)³³ and observed agonist off-rate by adding ^3H -naloxone in the presence or absence of excess **368** (Fig. 3f). ^3H -naloxone slowly bound to the receptor, presumably due to the high potency and low off-rate of MP (Fig. 3f). However, **368** bound the MP-bound receptor and substantially increased the off-rate of MP, which suggests that it interacts with the receptor contemporaneously with and destabilizes the interactions of the orthosteric agonist (Fig. 3f). However, this effect may also be possible because of the modulations in the naloxone off-rate, as discussed above (Fig. 3d). Finally, selective binding of the NAM to this structurally distinct inactive state of the receptor may explain the reduced potency of the modulator in agonist-only experiments (Fig. 2a and Extended Data Fig. 1i) and suggests that the extensive cooperation observed between naloxone and **368** may be taken advantage of in vivo.

Enhancement of the opioid reversal effects of naloxone

Molecules that increase the affinity and/or the residence time of naloxone for the receptor may have utility in reversing opioid overdoses. Therefore, given the substantial effects of **368** on naloxone affinity and kinetics, we aimed to characterize its ability to potentiate naloxone in vivo using mouse models. When intravenously administered at 10 mg kg^{-1} in mice, **368** enters the brain with moderate penetration (about 25% of maximum plasma levels, corresponding to >10-fold the affinity of **368**) with a relatively short observed half-life (0.51 h) (Extended Data Fig. 6a). We first tested the ability of **368** to potentiate low-dose naloxone reversal of morphine-induced antinociception. While naloxone is typically administered at doses of 1 or 10 mg kg^{-1} , subcutaneously (s.c.) to efficiently inhibit morphine-induced antinociception^{34–36}, the dose used here (0.1 mg kg^{-1} s.c.) was confirmed to have no significant antagonism (Fig. 4a, blue versus green). Although **368** alone had no significant impact on morphine-induced antinociception (Extended Data Fig. 6b), in the presence of low-dose naloxone, **368** significantly inhibited morphine-induced antinociception in a dose-dependent manner (Fig. 4a). The median dose of **368** to potentiate low-dose naloxone antagonism of morphine antinociception was $1.15 (0.03–4.04) \text{ mg kg}^{-1}$, s.c. We next tested the ability of **368**, in conjunction with the low dose (0.1 mg kg^{-1}) of naloxone, to inhibit morphine-mediated respiratory depression and hyperlocomotion using the Comprehensive Lab Animal Monitoring System (CLAMS) assay^{12,37}. Morphine (20 mg kg^{-1} , s.c.) significantly increased ambulations for more than 140 min (Fig. 4b) and decreased the breathing rate for up to 100 min (Fig. 4c). Pretreatment with the low dose of naloxone was ineffective in ameliorating morphine-induced hyperlocomotion (Fig. 4b, green versus blue), but significantly (if modestly) reduced morphine-induced respiratory depression (Fig. 4c, green versus blue). **368** itself did not change ambulation or breathing rate relative to vehicle (Extended Data Fig. 6c,d) or relative to morphine alone (Fig. 4b,c, blue versus red). However, it significantly enhanced low-dose naloxone inhibition of hyperlocomotion (Fig. 4b, pink versus green) and respiratory depression (Fig. 4c, pink versus green) induced by morphine in a dose-dependent manner maximal at the 100 mg kg^{-1} dose (Extended Data Fig. 6e,f). All subsequent experiments used this maximal dose of 100 mg kg^{-1} **368**.

Although the ability of **368** to potentiate low doses of naloxone against morphine is a clear demonstration of its activity in vivo, we were interested in testing the NAM for this same ability to work together with naloxone to reverse the opioid most responsible for the current overdose epidemic, fentanyl. Given the increased potency of fentanyl relative to morphine, we first screened submaximal doses of naloxone (0.3 mg kg^{-1} , Extended Data Fig. 6g; 0.5 mg kg^{-1} , Fig. 4d;

1.0 mg kg^{-1} , Extended Data Fig. 6h) against fentanyl (0.1 mg kg^{-1}) in the absence or presence of 100 mg kg^{-1} **368**. All doses of naloxone induced weak (0.3 mg kg^{-1} , Extended Data Fig. 6g) or not significant (0.5 mg kg^{-1} , Fig. 4d; 1.0 mg kg^{-1} , Extended Data Fig. 6h) effects against fentanyl-induced antinociception. Regardless of the dose of naloxone, treatment with **368** resulted in a significant enhancement of the ability of naloxone to reverse fentanyl-induced antinociception (Fig. 4d and Extended Data Fig. 6g,h, orange versus red).

We next tested the combined effects of the NAM and a low dose (0.1 mg kg^{-1} , s.c.) of naloxone for inhibition of morphine-induced conditioned place preference (CPP)^{12,37}. Pretreatment of mice with vehicle (~30 min) and the low dose of naloxone (~15 min) alone did not prevent significant morphine-induced CPP (Fig. 4e, central pair of bars) compared with CPP observed in the absence of low-dose naloxone (Fig. 4e, left pair of bars). By contrast, pretreatment with **368** (100 mg kg^{-1} , s.c., ~30 min) potentiated the μ OR antagonism produced by the low dose of naloxone to effectively eliminate morphine-mediated CPP (Fig. 4e, right pair of bars).

Finally, as **368** treatment potentiates low doses of naloxone in reversing morphine effects in a wide range of assays (Fig. 4a–c,e), we examined whether **368** pretreatment potentiates naloxone-precipitated withdrawal symptoms^{38,39}. We assessed whether those observed following administration of **368** (100 mg kg^{-1} , s.c.) and the low dose of naloxone (0.1 mg kg^{-1} , s.c.) are similar to the symptoms precipitated by treatment solely with conventional higher doses of naloxone (10 mg kg^{-1} , s.c.) alone. To that end, mice were first repeatedly given saline (control group 1) or morphine at escalating doses ($10–75 \text{ mg kg}^{-1}$, intraperitoneally (i.p.)) over the course of 5 days as utilized previously^{38,39}. Assessment of withdrawal symptoms on the fifth day followed treatment with the conventional high dose of naloxone, (10 mg kg^{-1} , group 2), the low dose of naloxone used for experiments herein (0.1 mg kg^{-1} , group 3) or the low dose of naloxone following treatment with **368** (100 mg kg^{-1} , group 4) (Fig. 4f–h). The battery of withdrawal-associated behaviours following naloxone treatment (summarized in Extended Data Table 4) demonstrated variable responses. Notably, the combined low-dose naloxone and NAM treatment did not potentiate the magnitude of withdrawal precipitated by a low dose of naloxone alone to the same levels of withdrawal symptoms as the conventional naloxone treatment. For some behaviours (for example, teeth chattering frequency, Fig. 4f), low-dose naloxone treatment alone had no effect relative to saline alone ($P = 0.76$). Moreover, the addition of **368** increased withdrawal symptoms relative to both ($P < 0.0001$, Tukey's post hoc test following one-way analysis of variance (ANOVA)), although notably significantly less than the response to high-dose naloxone treatment ($P < 0.0001$). For other measures, such as jumping frequency, low-dose naloxone treatment alone precipitated significant withdrawal symptoms (Fig. 4g), but was not significantly altered in the presence of **368** ($P = 0.66$). Of note, whereas low-dose and high-dose naloxone treatment induced significant diarrhoea in morphine-dependent mice (Fig. 4h), low-dose naloxone in combination with **368** treatment did not significantly change stool consistency relative to saline control ($P = 0.61$).

Discussion

Allosteric modulation of GPCR activity remains a promising pathway to develop therapeutics that work with endogenous signalling molecules and decrease side effects arising from both off-target effects and off-pathway activation events (for example, biased signalling)^{40–42}. Recent structures of allosteric modulator-bound family A and B GPCRs have highlighted the diversity of potential binding sites as well as the resulting effects on receptor activation pathway (or pathways)^{22,41,43–46}. The μ OR is an exception, whereby the total lack of NAM scaffolds that target the μ OR represents a largely unexploited area of both study and potential therapeutic intervention, especially given the current opioid overdose epidemic.

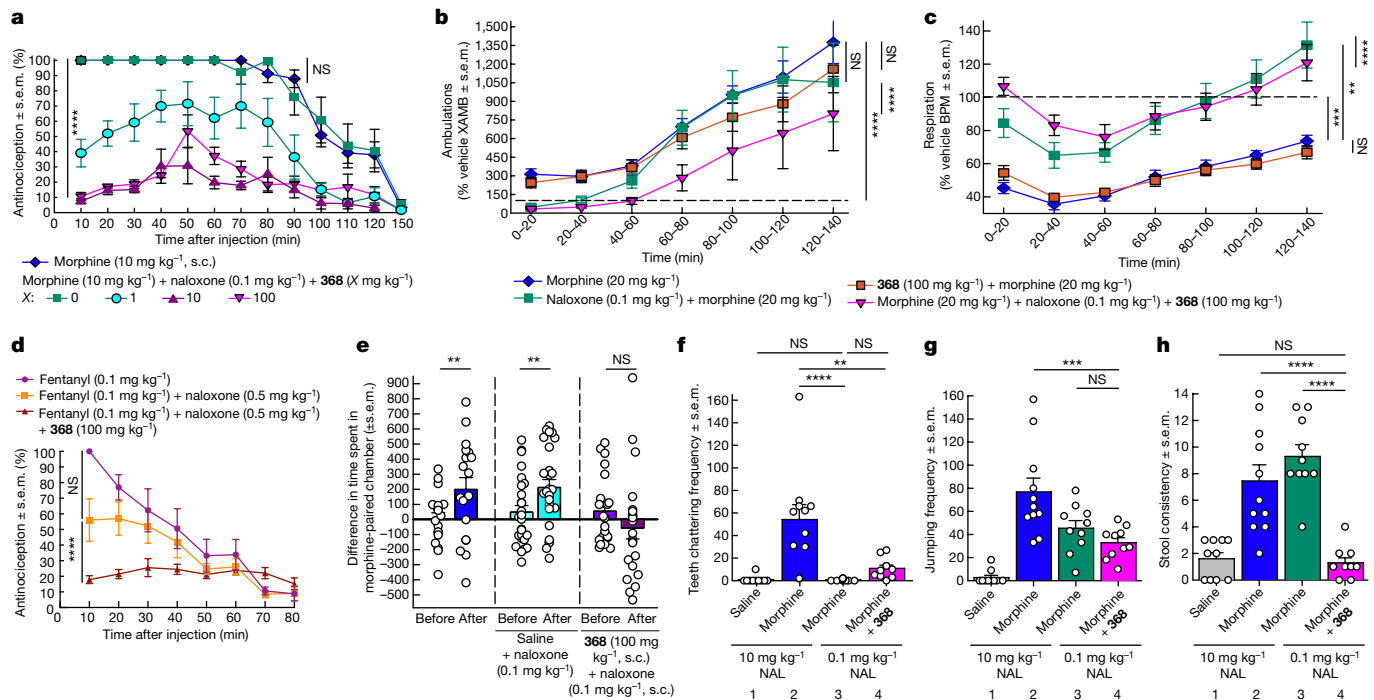


Fig. 4 | 368 potentiates naloxone activity in vivo. **a**, Antinociceptive time-course experiment (tail-flick analgesia with morphine) demonstrating that low doses of naloxone have no impact on morphine-induced antinociception, whereas increasing doses of **368** before morphine treatment in the presence of this low-dose naloxone results in substantial inhibition of morphine-induced antinociception. **b,c**, Although treatment with either low doses of naloxone or **368** on their own has no or only modest effects, we observed a similar enhancement of low-dose naloxone effects on hyperlocomotion (**b**) and respiratory depression (**c**) after co-administration with **368**. Data are displayed in 20-min bins as percentages relative to vehicle (XAMB, progressive ambulations; BPM, breaths per minute). **d**, Intermediate doses of naloxone are not able to significantly reverse fentanyl-induced antinociception (tail-flick analgesia), although addition of **368** resulted in a significant enhancement of this naloxone-induced reversal. **e**, Morphine produces significant CPP (left blue bars) that is not blocked with low doses of naloxone (~15 min, cyan central

bars), whereas pretreatment with **368** and low-dose naloxone eliminated morphine CPP (right purple bars). **f–h**, Naloxone (NAL) precipitation of withdrawal symptoms were measured, comparing conventional naloxone-induced effects (2) with the low doses used above without (3) and with (4) pretreatment with **368**. **f**, **368** with low-dose naloxone increases teeth chattering frequency relative to low-dose naloxone alone, although not to the same extent as full-dose naloxone. **g**, Low-dose naloxone alone causes substantial increases in jumping frequency that is not enhanced by **368**. **h**, Low-dose and high-dose naloxone causes significant diarrhoea in mice, although this response is inhibited by **368** such that there is no difference from saline control. See Methods for details on the statistical tests used and their results. All data are displayed as the mean \pm s.e.m. of cohort sizes described in the Methods. *P* values are denoted as follows: NS ($P > 0.05$), * $P \leq 0.05$, ** $P \leq 0.01$, *** $P \leq 0.001$ and **** $P \leq 0.0001$.

We showed that DEL hits from this screening strategy can be useful compounds for investigating mechanisms of negative allosteric modulation of the μ OR, which then lead directly to useful in vivo properties. We showed that **368** acts as a NAM by both enhancing naloxone binding to the receptor (increasing its affinity and decreasing its off-rate) and independently stabilizing an inactive conformation of the extracellular vestibule including TM7 and ECL3. This allosteric inhibition by **368** increased the off-rate of orthosteric agonists. Although **368** had minimal effect on its own in mouse behavioural assays, it potentiated naloxone-induced inhibition of various opioid effects, including morphine-induced and fentanyl-induced antinociception, hyperlocomotion and respiratory depression (Fig. 4). It enhanced the antagonism of low-dose naloxone while not resulting in the same extent of withdrawal effects observed for conventional, high-dose naloxone treatment (Fig. 4f–h). Although these results demonstrate negative allosteric modulation of the μ OR, future work is anticipated to further explore the optimal relationship between subthreshold naloxone and **368** co-treatment needed to best replicate the therapeutic outcomes for current naloxone dosing strategies. Likewise, future development of **368** will focus on extending its half-life and brain-penetrating properties and improving its potency to increase its effectiveness against even highly potent opioid (for example, fentanyl) effects.

The targeted screening strategy used herein can potentially be used to generate negative small-molecule allosteric modulators of

other GPCRs. Our selection strategy is not just based on the presence of allosteric pockets⁴⁷ but necessitates their change in structure after an alteration in the activation state of the receptor. In other words, the strategy targets sites that are strongly correlated with receptor activation and signalling. The potential challenges of the molecules discovered here present opportunities for further selection. Future studies should anticipate the probe dependence we observed for **368** and may even be able to select for modulators that are specific for orthosteric molecules of interest. Finally, our selection methodology enables the detection of molecules that bind to any conformation that is present within the active or inactive ensembles, as evidenced by the distinct inactive conformation of the receptor compared with previous antagonist-bound structures^{29,30} (Fig. 3e). Selecting for ensembles of states with DEL screens is a way of exploiting this intrinsic plasticity of proteins, especially GPCRs.

Online content

Any methods, additional references, Nature Portfolio reporting summaries, source data, extended data, supplementary information, acknowledgements, peer review information; details of author contributions and competing interests; and statements of data and code availability are available at <https://doi.org/10.1038/s41586-024-07587-7>.

1. Jamison, R. N. & Mao, J. Opioid analgesics. *Mayo Clin. Proc.* **90**, 957–968 (2015).
2. O'Donnell, J. K., Halpin, J., Mattson, C. L., Goldberger, B. A. & Gladden, R. M. Deaths involving fentanyl, fentanyl analogs, and U-47700—10 states, July–December 2016. *MMWR Morb. Mortal. Wkly Rep.* **66**, 1197–1202 (2017).
3. Centers for Disease Control and Prevention. Vital signs: overdoses of prescription opioid pain relievers—United States, 1999–2008. *MMWR Morb. Mortal. Wkly Rep.* **60**, 1487–1492 (2011).
4. Rudd, R. A. et al. Increases in heroin overdose deaths—28 states, 2010 to 2012. *MMWR Morb. Mortal. Wkly Rep.* **63**, 849–854 (2014).
5. National Academies of Sciences, Engineering, and Medicine. *Pain Management and the Opioid Epidemic: Balancing Societal and Individual Benefits and Risks of Prescription Opioid Use* (National Academies Press, 2017).
6. Abdelal, R. et al. Real-world study of multiple naloxone administration for opioid overdose reversal among bystanders. *Harm. Reduct. J.* **19**, 49 (2022).
7. Thompson, G. L. et al. Biased agonism of endogenous opioid peptides at the μ -opioid receptor. *Mol. Pharmacol.* **88**, 335–346 (2015).
8. Benarroch, E. E. Endogenous opioid systems: current concepts and clinical correlations. *Neurology* **79**, 807–814 (2012).
9. De Neve, J. et al. Comprehensive overview of biased pharmacology at the opioid receptors: biased ligands and bias factors. *RSC Med. Chem.* **12**, 828–870 (2021).
10. Wang, Y. et al. Structures of the entire human opioid receptor family. *Cell* <https://doi.org/10.1016/j.cell.2022.12.026> (2023).
11. Rasmussen, K., White, D. A. & Acri, J. B. NIDA's medication development priorities in response to the opioid crisis: ten most wanted. *Neuropsychopharmacology* **44**, 657–659 (2019).
12. Fauzzi, A. et al. Structure-based design of bitopic ligands for the μ -opioid receptor. *Nature* **613**, 767–774 (2023).
13. Bueno, A. B. et al. Structural insights into probe-dependent positive allosterism of the GLP-1 receptor. *Nat. Chem. Biol.* **16**, 1105–1110 (2020).
14. Vaysse, P. J.-J., Gardner, E. L. & Zukin, S. Modulation of rat brain opioid receptors by cannabinoids. *J. Pharmacol. Exp. Ther.* **241**, 534–539 (1987).
15. Rothman, R. B. et al. Salvinorin A: allosteric interactions at the μ -opioid receptor. *J. Pharmacol. Exp. Ther.* **320**, 801–810 (2007).
16. Franzini, R. M. & Randolph, C. Chemical space of DNA-encoded libraries: miniperspective. *J. Med. Chem.* **59**, 6629–6644 (2016).
17. Halford, B. How DNA-encoded libraries are revolutionizing drug discovery. *Chemical & Engineering News* (19 June 2017).
18. Gironda-Martínez, A., Donckeile, E. J., Samain, F. & Neri, D. DNA-encoded chemical libraries: a comprehensive review with successful stories and future challenges. *ACS Pharmacol. Transl. Sci.* **4**, 1265–1279 (2021).
19. Ahn, S. et al. Small-molecule positive allosteric modulators of the β_2 -adrenoceptor isolated from DNA-encoded libraries. *Mol. Pharmacol.* **94**, 850–861 (2018).
20. Ahn, S. et al. Allosteric “beta-blocker” isolated from a DNA-encoded small molecule library. *Proc. Natl. Acad. Sci. USA* **114**, 1708–1713 (2017).
21. Liu, X. et al. Mechanism of intracellular allosteric β_2 AR antagonist revealed by X-ray crystal structure. *Nature* **548**, 480–484 (2017).
22. Liu, X. et al. Mechanism of β_2 AR regulation by an intracellular positive allosteric modulator. *Science* **364**, 1283–1287 (2019).
23. Gregorio, G. G. et al. Single-molecule analysis of ligand efficacy in β_2 AR–G-protein activation. *Nature* **547**, 68–73 (2017).
24. Hilger, D. et al. Structural insights into differences in G protein activation by family A and family B GPCRs. *Science* **369**, eaba3373 (2020).
25. Olsen, R. H. J. et al. TRUPATH, an open-source biosensor platform for interrogating the GPCR transducerome. *Nat. Chem. Biol.* **16**, 841–849 (2020).
26. Livingston, K. E. & Traynor, J. R. Allostery at opioid receptors: modulation with small molecule ligands. *Br. J. Pharmacol.* **175**, 2846–2856 (2018).
27. Che, T. et al. Structure of the nanobody-stabilized active state of the kappa opioid receptor. *Cell* **172**, 55–67.e15 (2018).
28. Che, T. et al. Nanobody-enabled monitoring of kappa opioid receptor states. *Nat. Commun.* **11**, 1145 (2020).
29. Robertson, M. J. et al. Structure determination of inactive-state GPCRs with a universal nanobody. *Nat. Struct. Mol. Biol.* <https://doi.org/10.1038/s41594-022-00859-8> (2022).
30. Manglik, A. et al. Crystal structure of the μ -opioid receptor bound to a morphinan antagonist. *Nature* **485**, 321–326 (2012).
31. Huang, W. et al. Structural insights into μ -opioid receptor activation. *Nature* **524**, 315–321 (2015).
32. Koehl, A. et al. Structure of the μ opioid receptor–G_i protein complex. *Nature* **558**, 547–552 (2018).
33. Várdai, A. et al. Mitrugynine/corynantheidine pseudoindoxyls as opioid analgesics with mu agonism and delta antagonism, which do not recruit β -arrestin-2. *J. Med. Chem.* **59**, 8381–8397 (2016).
34. Smits, S. E. Antagonism by naloxone of morphine-induced single-dose dependence and antinociception in mice. *Res. Commun. Chem. Pathol. Pharmacol.* **15**, 689–696 (1976).
35. Bloom, A. S., Dewey, W. L., Harris, L. S. & Brosius, K. K. The correlation between antinociceptive activity of narcotics and their antagonists as measured in the mouse tail-flick test and increased synthesis of brain catecholamines. *J. Pharmacol. Exp. Ther.* **198**, 33–41 (1976).
36. Székely, J. I., Dunai-Kovács, Z., Miglécz, E., Rónai, A. Z. & Bajusz, S. In vivo antagonism by naloxone of morphine, beta-endorphin and a synthetic enkephalin analog. *J. Pharmacol. Exp. Ther.* **207**, 878–883 (1978).
37. Chakraborty, S. et al. Oxidative metabolism as a modulator of kratom’s biological actions. *J. Med. Chem.* **64**, 16553–16572 (2021).
38. Wilson, L. L. et al. Lyophilized kratom tea as a therapeutic option for opioid dependence. *Drug Alcohol Depend.* **216**, 108310–108318 (2020).
39. Wilson, L. L. et al. Kratom alkaloids, natural and semi-synthetic, show less physical dependence and ameliorate opioid withdrawal. *Cell. Mol. Neurobiol.* **41**, 1131–1143 (2021).
40. Kandasamy, R. et al. Positive allosteric modulation of the mu-opioid receptor produces analgesia with reduced side effects. *Proc. Natl. Acad. Sci. USA* **118**, e2000017118 (2021).
41. Draper-Joyce, C. J. et al. Positive allosteric mechanisms of adenosine A₁ receptor-mediated analgesia. *Nature* **597**, 571–576 (2021).
42. Slosky, L. M. et al. β -arrestin-biased allosteric modulator of NTSR1 selectively attenuates addictive behaviors. *Cell* **181**, 1364–1379.e14 (2020).
43. Persechino, M., Hedderich, J. B., Kolb, P. & Hilger, D. Allosteric modulation of GPCRs: from structural insights to in silico drug discovery. *Pharmacol. Ther.* **237**, 108242 (2022).
44. Krumm, B. E. et al. Neurotensin receptor allosterism revealed in complex with a biased allosteric modulator. *Biochemistry* **62**, 1233–1248 (2023).
45. Cong, Z. et al. Molecular insights into ago-allosteric modulation of the human glucagon-like peptide-1 receptor. *Nat. Commun.* **12**, 3763 (2021).
46. Xu, J. et al. Structural and dynamic insights into supra-physiological activation and allosteric modulation of a muscarinic acetylcholine receptor. *Nat. Commun.* **14**, 376 (2023).
47. Hedderich, J. B. et al. The pocketome of G-protein-coupled receptors reveals previously untargeted allosteric sites. *Nat. Commun.* **13**, 2567 (2022).

Publisher's note Springer Nature remains neutral with regard to jurisdictional claims in published maps and institutional affiliations.

Springer Nature or its licensor (e.g. a society or other partner) holds exclusive rights to this article under a publishing agreement with the author(s) or other rightsholder(s); author self-archiving of the accepted manuscript version of this article is solely governed by the terms of such publishing agreement and applicable law.

© The Author(s), under exclusive licence to Springer Nature Limited 2024

Methods

Purification of μOR and variants

Purification of mouse μOR from sf9 cells. Mouse μOR was grown and purified as previously described³². Mouse μOR with an amino-terminal Flag and carboxy-terminal hexahistidine tag was expressed as previously described³² using the baculovirus method in *Spodoptera frugiperda* (Sf9) cells (Expression Systems). Naloxone was added to 10 μM final concentration after infection, and cells were collected 48 h after infection and stored at -80 °C for later purification. μOR was extracted from membranes with 0.8% n-dodecyl-β-D-malopyranoside (DDM; Anatrace), 0.08% cholesterol hemisuccinate (CHS) and 0.3% 3-((3-cholamidopropyl) dimethylammonio)-1-propanesulfonate (CHAPS; Anatrace) in 20 mM HEPES pH 7.5, 500 mM NaCl, 30% glycerol, 5 mM imidazole, 10 μM naloxone and the protease inhibitors benzamidine and leupeptin, along with benzonase (Sigma-Aldrich) to degrade cellular DNA. Cells were dounced 30 times on ice and the membranes were allowed to solubilize in the detergent for 2 h with stirring at 4 °C, followed by centrifugation for 40 min at 14,000 r.p.m. to pellet cell debris. The supernatant was applied to nickel-chelating sepharose resin and bound to resin with end-over-end shaking for 2 h at 4 °C. The resin was then batch washed 4 times followed by washing with 10 column volumes on-column with nickel wash buffer composed of 20 mM HEPES pH 7.4, 500 mM NaCl, 0.1% DDM, 0.01% CHS, 0.03% CHAPS, 5 mM imidazole, 10 μM naloxone and the protease inhibitors leupeptin and benzamidine. The nickel-pure μOR was then eluted in the same buffer with 250 mM imidazole. The nickel elution was initially exchanged to lauryl maltose neopentyl glycol (L-MNG; Anatrace) detergent by incubating with 0.5% L-MNG, 0.17% glycol-diogenin (GDN; Anatrace) and 0.067% CHS overnight at 4 °C. Next, 2 mM CaCl₂ was added and subsequently applied to M1 anti-Flag immunoaffinity resin. The M1-bound receptor was first washed with 20 mM HEPES pH 7.4, 500 mM NaCl, 0.1% MNG, 0.033% GDN, 0.0133% CHS, 2 mM CaCl₂ and 10 μM naloxone. The protein was then washed with 10 column volumes of 20 mM HEPES pH 7.4, 100 mM NaCl, 0.005% MNG, 0.0017% GDN, 0.00067% CHS and 2 mM CaCl₂ followed by elution with 20 mM HEPES pH 7.4, 100 mM NaCl, 0.003% MNG, 0.001% GDN, 0.0004% CHS, 5 mM EDTA and Flag peptide. Multimers and dimers of the receptor were removed using size-exclusion chromatography on a S200 10/300 Increase gel filtration column (GE Healthcare) equilibrated with 20 mM HEPES pH 7.4, 100 mM NaCl, 0.01% MNG and 0.001% CHS. Pure, monomeric apo μOR was spin-concentrated to about 150 μM, flash-frozen in liquid nitrogen and stored at -80 °C until further use.

The μOR-κOR(ICL3) used for determination of the inactive-state structure was purified in an identical fashion for mouse μOR described above. Two point mutations in ICL3 (M264L and K269R) are present in the construct to enable binding to the κOR-specific Nb6 as previously described²⁹.

Purification of human μOR from Expi293 cells. The gene for the full-length human μOR was cloned into a vector for inducible expression in Expi293F cells (Thermo Fisher) with N-terminal HA signal peptide and Flag tags and a C-terminal hexahistidine tag. This construct was transfected into Expi293F cells constitutively expressing the tetracycline repressor (Thermo Fisher) with an Expifectamine transfection kit (Thermo Fisher) following the manufacturers direction's. Induction of receptor expression was done 2 days after transfection with doxycycline (4 μg ml⁻¹ and 5 mM sodium butyrate) in the presence of 10 μM naloxone. Pellets were collected and frozen at -80 °C about 30 h after induction for subsequent protein purification. Cells were dounced and membranes solubilized with 20 mM HEPES pH 7.5, 100 mM NaCl, 20% glycerol, 1% L-MNG, 0.1% CHS, 10 μM naloxone, the protease inhibitors leupeptin and benzamidine, and benzonase, followed by purification on anti-Flag immunoaffinity resin as described above. Multimers and

dimers of the receptor were removed by size-exclusion chromatography on an S200 10/300 Increase gel filtration column (GE Healthcare) equilibrated with 20 mM HEPES pH 7.4, 100 mM NaCl, 0.01% MNG and 0.001% CHS. Pure, monomeric apo μOR was spin-concentrated to about 150 μM, flash-frozen in liquid nitrogen and stored at -80 °C until further use.

Expression and purification of heterotrimeric G proteins

Heterotrimeric G_i was expressed in *Trichoplusia ni* using the BestBac method (Expression Systems) and purified as previously described^{32,48}. In brief, *T. ni* cells were infected with one virus encoding the wild-type human Gα_i subunit and another encoding the wild-type human β₁γ₂ subunits with a histidine tag inserted at the N terminus of the β-subunit. Cells were collected 48 h after infection and lysed with hypotonic buffer. Heterotrimeric Gα_iβ₁γ₂ proteins were extracted in buffer containing 1% sodium cholate and 0.05% DDM. The heterotrimer was purified using nickel-chelating sepharose chromatography while removing cholate. Human rhinovirus 3C protease (3C protease) was added to cleave off the histidine tag overnight at 4 °C on-column. The flow through was collected and dephosphorylated with lambda protein phosphatase (NEB), calf intestinal phosphatase (NEB) and Antarctic phosphatase (NEB) in the presence of 1 mM MnCl₂. The heterotrimer was further purified by ion-exchange chromatography on a MonoQ 10/100 GL column (GE Healthcare) in 20 mM HEPES pH 7.5, 1 mM MgCl₂, 0.05% DDM, 100 μM TCEP and 20 μM GDP and eluted with a linear NaCl gradient from 50 to 500 mM. The purified heterotrimer was collected and dialysed into 20 mM HEPES pH 7.5, 100 mM NaCl, 0.02% DDM, 100 μM TCEP and 20 μM GDP overnight at 4 °C, followed by concentration to <250 μM, addition of 20% glycerol and flash-freezing in liquid nitrogen and storage at -80 °C until further use.

Purification of Nb6

Nb6 was grown and purified in a similar manner to that previously described²⁹. In brief, BL21 *Escherichia coli* were transformed with Nb6 plasmid²⁸, and single colonies were picked into small-scale starter cultures in LB with 100 μg ml⁻¹ ampicillin, grown overnight at 37 °C. The starter culture was used to inoculate larger cultures of TB supplemented with 100 μg ml⁻¹ ampicillin, which were grown to an optical density of 600 nm = 0.7. IPTG was added to 1 mM to induce expression overnight at room temperature. Pellets were collected and flash-frozen for later purification.

Pellets were resuspended with 50 mM Tris pH 8.0, 0.5 mM EDTA and 20% w/v sucrose (TES) buffer at a ratio of 2 ml buffer per gram of pellet mass in the presence of protease inhibitor cocktail and shaken for 1 h at 4 °C. An additional 4 ml of TES buffer diluted 1:4 in water per gram of pellet was added; the mixture was shaken for an additional hour at 4 °C. Cell debris was pelleted by centrifugation at 18,000 r.p.m. for 15 min, and the resulting supernatant was removed and bound to nickel-chelating sepharose resin in batch for 1.5 h at 4 °C with gentle shaking with 5 mM imidazole supplemented to the solution. The Nb6-bound resin was then loaded into a gravity column and washed with 20 mM HEPES pH 7.4 and 100 mM NaCl followed by washing with the same buffer with 500 mM NaCl. The Nb6 was eluted in the same high-salt buffer with 250 mM imidazole. Nickel-pure Nb6 was then dialysed overnight into 20 mM HEPES with 100 mM NaCl, followed by final purification by size-exclusion chromatography on a S200 10/300 Increase column in the same buffer. Nb6 was concentrated and flash-frozen in liquid nitrogen for further experiments.

Preparation of samples for DEL selection

μOR-naloxone formation. Purified μOR (above) was incubated with excess naloxone for 1 h at room temperature before selection experiments in 20 mM HEPES pH 7.4, 100 mM NaCl, 0.003% MNG, 0.001% GDN and 0.0004% CHS.

μOR-G_i-met-enkephalin complex formation. μOR-G_i complex was formed in a similar manner to that previously described^{32,49}. In brief, excess met-enkephalin peptide (MedChemExpress) was added to purified μOR (described above) and incubated at room temperature for 1 h. Concurrently, 1% L-MNG with 0.1% CHS was added to G_i purified in DDM to exchange detergent on ice for 1 h. The two reactions were mixed to a final molar ratio of 1:1.5 μOR:G_i and incubated at room temperature for 1 h. Apyrase was added and the reaction was further incubated on ice for 2 h. Next, 2 mM CaCl₂ was added to the reaction before adding to M1 anti-Flag resin for 20 min. The column was washed with 20 mM HEPES pH 7.4, 100 mM NaCl, 0.003% MNG, 0.001% GDN, 0.0004% CHS, 5 μM met-enkephalin and 2 mM CaCl₂, followed by elution in the same buffer with 5 mM EDTA, replacing the CaCl₂ and Flag peptides. After removing excess unbound G_i heterotrimer, excess uncoupled μOR was removed by size-exclusion chromatography with a S200 10/300 Increase column into 20 mM HEPES pH 7.4 and 100 mM NaCl, 0.003% MNG, 0.001% GDN, 0.0004% CHS, 100 μM TCEP and 1 μM met-enkephalin. μOR-G_i-met-enkephalin complex was spin-concentrated to about 25 μM and flash-frozen in liquid nitrogen after adding 15% glycerol.

DEL selection

Target preparation. The two samples of μOR-naloxone or μOR-G_i-met-enkephalin were diluted to 2 μM final concentration in W1: 20 mM HEPES pH 7.4, 150 mM NaCl, 100 μM TCEP, 0.1% hsDNA (Thermo Fisher Scientific), 0.02% MNG, 0.002% CHS and 20 μM ligand (naloxone and met-enkephalin, respectively). A third blank sample (no protein control) was made with the same buffer in the absence of ligand. Next, 300 μl of HisPur Ni-NTA magnetic beads (Thermo Fisher Scientific) as slurry were washed with water followed by splitting into three batches and washing with the three respective buffers made above. Washing with buffer was repeated two additional times. Next, 300 μl of 2 μM targets (specified above) and 300 μl buffer without agonist was incubated with the respective magnetic Ni-NTA resin for 30 min with mixing to bind targets to resin. Each of the 3 samples was then split into 3 100 μl aliquots corresponding to each of the 3 rounds of selection.

First round of selection. Any unbound target was removed from the 3 100 μl targets by washing with 200 μl respective wash buffer (described above). The 3 DEL samples (G1, G2 and G3) provided by WuXi (10 μl) were resuspended with 90 μl of the respective wash buffers above for the 3 conditions and then applied to the 3 targets bound to magnetic resin and incubated with shaking at room temperature for 1.5 h to bind to the target(s). Reactions were spun briefly to settle the resin, followed by washing all with 200 μl of the above-described respective buffer. The 3 selections were then washed again with 200 μl of the same buffers with lower detergent concentrations (0.001% MNG and 0.0001% CHS) and lower ligand concentrations (500 nM) (W2). The 3 selections were then washed with 200 μl of the same respective buffers in the absence of detergent and even further lower ligand concentration (100 nM) (W3) to minimize detergent and ligand carry-over between rounds. The resin with target (and bound library molecules) was then resuspended in 100 μl of the respective last wash buffer and heated at 95 °C for 10 min to elute bound library components but leave the receptor bound to resin. The heat-denatured mixture was spun down and the supernatant removed from the resin. Next, 10 μl of each of the 3 selections was saved for later analysis, and 90 μl was reserved for the next round of selection.

Second round of selection. Another 100 μl aliquot of target-bound magnetic resin was washed with 200 μl respective W1 buffer to remove unbound target. The 3 samples of resin were then resuspended in 90 μl respective W1, to which the 90 μl of reserved round 1 DEL selection was added and incubated with shaking at room temperature for 1.5 h. Reactions were spun briefly to settle the resin, followed by washing

with 200 μl respective W1 buffer. The 3 selections were then washed again with 200 μl of respective W2 buffer, followed by 200 μl of respective W3 buffer. The resin with target (and bound library molecules) was then resuspended in 100 μl respective W3 and heated at 95 °C for 10 min to elute bound library components but leave the receptor bound to resin. The heat-denatured mixture was spun down and the supernatant removed from the resin. Finally, 50 μl of each of the 3 selections was saved for later analysis, and 50 μl was reserved for the next round of selection.

Third round of selection. Another 100 μl aliquot of target-bound magnetic resin was washed with 200 μl respective W1 buffer to remove unbound target. The 3 samples of resin were then resuspended in 50 μl respective W1, to which the 50 μl of reserved round 2 DEL selection was added and incubated with shaking at room temperature for 1.5 h. Reactions were spun briefly to settle the resin, followed by washing with 200 μl respective W1 buffer. The 3 selections were then washed again with 200 μl of respective W2 buffer, followed by 200 μl of respective W3 buffer. The resin with target (and bound library molecules) was then resuspended in 100 μl respective W3 and heated at 95 °C for 10 min to elute bound library components but leave the receptor bound to resin. The heat-denatured mixture was spun down and the supernatant removed from the resin. All of the final (third) round of selection supernatant for all 3 conditions was saved for subsequent sequencing and enrichment analysis.

Preparation of μOR membranes

Cell membranes containing mouse μOR were generated by infecting Sf9 cells in an identical manner to that described above for protein purification. Sf9 cells expressing μOR were resuspended in cold lysis buffer composed of 10 mM HEPES pH 7.4, 10 mM MgCl₂ and 20 mM KCl with the protease inhibitors leupeptin and benzamidine, and cComplete EDTA-free protease inhibitor cocktail tablets (Sigma-Aldrich). The lysed cells were spun at 45,000 r.p.m. for 45 min to pellet membranes. The supernatant was removed and membrane pellets were resuspended in cold lysis buffer followed by douncing about 30 times on ice. The dounced membranes were spun again at 45,000 r.p.m. for 45 min. The pellets were resuspended in cold lysis buffer with the addition of benzonase and dounced an additional 30 times, followed by a spin at 45,000 r.p.m. for 45 min. Membranes were resuspended in the same lysis buffer as described above in the presence of 1 M NaCl and dounced about 30 times and pelleted. Finally, membranes were washed with the original lysis buffer, dounced and pelleted. Final washed membranes were resuspended to 2 g original pellet mass per 1 ml in lysis buffer. The resulting μOR-containing membranes were flash-frozen for subsequent radioligand-binding experiments.

Radioligand-binding experiments

Membrane-binding experiments. μOR-containing insect cell membranes were diluted 1:1,000 in 20 mM HEPES pH 7.4, 100 mM NaCl and 0.05% BSA. For saturation-binding experiments, membranes were incubated with a serial dilution of ³H-naloxone (50.3 Ci mmol⁻¹; Perkin Elmer) and allosteric modulators at different constant concentrations for 1.5 h at room temperature with shaking. For competition-binding experiments, membranes were incubated with 2 nM ³H-naloxone and serially diluted allosteric modulators for 1.5 h at room temperature with shaking. Following incubation, membranes were rapidly bound to double-thick 90 × 120 mm glass fibre printed Filtermat B filters (Perkin Elmer) and washed with cold binding buffer (20 mM HEPES pH 7.4, 100 mM NaCl) using a MicroBeta Filtermat-96 cell harvester (Perkin Elmer). ³H-naloxone-bound membranes on Filtermats were measured with a MicroBeta counter (Perkin Elmer) after addition of MultiLex B/HS melt-on scintillator sheets (Perkin Elmer). Data values were plotted after normalizing total counts per min to the highest and lowest values.

Article

Kinetic SPA binding. Copper His-Tag PVT slurred resin (Perkin Elmer) was added 1:1 v/v with 40 mM HEPES pH 7.4, 200 mM NaCl, 0.02% MNG, 0.002% CHS and 0.1% BSA to match buffer with the receptor. For the ³H-naloxone on-rate experiment (MP off-rate experiment), purified μOR in detergent was diluted to 40 nM in 20 mM HEPES pH 7.4, 100 mM NaCl, 0.01% MNG, 0.001% CHS and 0.05% BSA in the presence or absence of slight (60 nM) excess high affinity orthosteric agonist (MP). Next, 25 μl of receptor solution was incubated with 50 μl resin slurry in buffer for 1 h with shaking at room temperature. ³H-naloxone was diluted to 200 nM in 20 mM HEPES pH 7.4, 100 mM NaCl, 0.01% MNG, 0.001% CHS, and 0.05% BSA in the presence or absence of 100 μM **368** NAM compound and in the presence or absence of 200 μM cold naloxone. 25 μl of the ³H-naloxone solutions was added to the 75 μl receptor–SPA resin mixtures to initiate radioligand binding to the receptor and the solutions were immediately read on a MicroBeta counter at various time points for about 5 h. Data were normalized to total counts observed for the non-specific binding condition and the maximum counts observed in the absence of MP and cold naloxone.

For the ³H-naloxone off-rate experiment, purified μOR in detergent was diluted to 40 nM in 20 mM HEPES pH 7.4, 100 mM NaCl, 0.01% MNG, 0.001% CHS, and 0.05% BSA with 50 nM ³H-naloxone in the presence or absence of 100 μM **368**. Excess cold naloxone (200 μM) was added at $t = 0$ and counts were measured at various time points for about 30 min. Counts were normalized to 0% (excess cold naloxone, no **368**) and 100% (no cold naloxone, no **368**) throughout the time course.

Chemical synthesis

Reagents were purchased from Sigma-Aldrich Chemicals, Ambeed, ChemScene and Chemimpex and used as received. All reactions were performed under argon atmosphere unless otherwise specified. While performing synthesis, reaction mixtures were purified by silica gel flash chromatography on E. Merck 230–400 mesh silica gel 60 using a Teledyne ISCO CombiFlash Rf instrument with UV detection at 280 and 254 nm. RediSep Rf silica gel normal phase columns were used with a gradient range of 0–80% ethyl acetate in hexane. Reported yields are isolated yields after purification of each intermediate. Final clean (purity $\geq 95\%$, LC–MS Agilent 1100 Series LC/MSD) compounds were used for the study. NMR spectra were collected using a Varian 400 MHz and 500 MHz NMR instrument at the NMR facility of Washington University School of Medicine in St Louis collected using Bruker Top-spin software (Bruker Topspin 3.5 pl 6). Chemical shifts are reported in parts per million relative to residual solvent peaks at the nearest 0.01 for proton and 0.1 for carbon (CDCl₃ 1H: 7.26, 13 C: 77.1). Peak multiplicity is reported for NMR spectra processed using MestreNova software (v.14.2.0), namely, s, singlet, d, doublet, t, triplet, q, quartet and m, multiplet. Coupling constant (J) values are expressed in Hz. Mass spectra were obtained at the St Louis College of Pharmacy using an Agilent 1100 Series LC/MSD by electrospray ionization with a gradient elution program (Ascentis Express Peptide C18 column, acetonitrile/water 5/95/95/5, 5 min, 0.05% formic acid) and UV detection (214 nM/254 nM). High-resolution mass spectra were obtained using a Bruker 10 T APEX-Qe FTICR-MS and the accurate masses are reported for the molecular ion [M+H]⁺. Optical rotation data were recorded on a Perkin-Elmer Model 341 Polarimeter. For determination of enantiomeric excess for the individually synthesized enantiomers, samples were analysed using a Diacel ChiraPak IC, 250 (length) × 4.6 (inner diameter) mm column on an Agilent 1260 SFC using a 2 ml min⁻¹ flow rate in a 60% methanol solution with 0.1% DEA as the mobile phase, CO₂ modifier with observation at 220 nm for the traces presented in Extended Data Fig. 3b–d. Detailed experiments and characterization of the new compounds are included below. See Supplementary Information for detailed synthetic schemes, synthetic steps and compound characterization data, including HRMS, NMR, chiral supercritical fluid chromatography and optical rotation.

GTP turnover assay

The GTP turnover assay was performed using a modified version of the GTPase-GLO assay (Promega) as previously described^{23,24}. Purified μOR was diluted to 1 μM (2 μM for basal activity experiments) in 20 mM HEPES pH 7.4, 100 mM NaCl, 0.01% L-MNG, 0.001% CHS and 20 μM GTP in the presence of various orthosteric (20 μM met-enkephalin, 20 μM naloxone, 20 μM MP, 20 μM DAMGO or 20 μM BU72) and allosteric (serially diluted or at excess concentrations of 20 μM for **368**) ligands and incubated for 1.5 h at room temperature. Concurrently, G_i purified in DDM was exchanged by incubating with 1% L-MNG and 0.1% CHS for 1 h on ice. The exchanged G_i was then diluted to 1 μM in 20 mM HEPES pH 7.4, 100 mM NaCl, 0.01% L-MNG, 0.001% CHS, 20 μM GDP, 200 μM TCEP and 20 mM MgCl₂. Equal volumes of receptor solutions and G_i solution were mixed and incubated at room temperature for 60 min (agonist-bound receptor experiments) or 90 min (apo receptor experiments) with gentle shaking. Controls include mixing equal volumes of both buffers (total initial GTP) and equal volumes of 1 μM G_i solution and receptor buffer (intrinsic G protein turnover). Equal volume of GTPase-Glo reagent supplemented with 10 μM ADP in 20 mM HEPES pH 7.4, 100 mM NaCl, 0.01% MNG and 0.001% CHS was added and incubated with gentle shaking for 30 min, followed by addition of further equal volume of detection reagent. After brief (10 min) incubation, luminescence was measured using a MicroBeta counter.

Cell-based cAMP assay

HEK293 cells stably expressing the Epac1-based FRET cAMP biosensor (PMID: 23374187) were transfected with a pcDNA3.1(+)-neo-based plasmid encoding a Flag-tagged human μOR using Fugene6 (Promega E2691) according to the manufacturer's instructions. Cells were maintained in growth medium (DMEM (Gibco 10566016) supplemented with 10% fetal bovine serum (Gibco, 10270106), 1% sodium pyruvate (Gibco, 11360039), 1% MEM non-essential amino acids (Gibco, 11140068) and 1% penicillin–streptomycin solution (Gibco, 15140122)) supplemented with 50 μg ml⁻¹ zeocin (for selection of the Epac1-based FRET cAMP biosensor) and 500 μg ml⁻¹ G418 (for selection of Flag-tagged μOR). Following limited dilution cloning in growth medium containing zeocin and G418, single colonies were picked and tested for their ability to decrease forskolin-induced cAMP formation after activation with met-enkephalin (as described below). One clone was chosen, propagated and used for subsequent testing.

The day before assaying, cells were seeded at 100 μl per well in a black poly-L-lysine-coated 96-well plate at 30,000 cells per well. Before assaying, cells were washed with 100 μl HBSS buffer (HBSS (Gibco, 14025), 20 mM HEPES pH 7.5, 1 mM CaCl₂, 1 mM MgCl₂ and 0.1% BSA) and replaced with 25 μl HBSS buffer in each well. For testing of **368** to inhibit agonist-induced response cAMP alone, **368** was added to wells at different concentrations (25 μl, 4× final concentration) and preincubated for 20 min. Likewise, for testing of the NAM to potentiate the effect of naloxone, mixtures of **368** and naloxone at different concentrations were added to wells and preincubated for 20 min. Then forskolin, diluted in a volume of 25 μl, was added to all wells to final a concentration of 15 μM and incubated for 20 min while following the change in FRET ratio between CFP and YFP as a measure of cAMP formation using an Envision plate reader (PMID: 23374187). Orthosteric agonists, diluted to an EC₅₀ in forskolin buffer (corresponding to a final concentration of 15 μM forskolin), were added at a volume of 25 μl to wells, and the changes in cAMP formation measured for 1 h. For determining orthosteric agonist potencies at the μOR alone, buffer only was added in the preincubation step. For quantification of cAMP levels, the AUC from the point of orthosteric agonist addition was calculated for each well. Concentration–response curves were fitted by nonlinear regression to a four-parameter logistic curve using GraphPad Prism 9 after plotting the cAMP AUC as a function of compound concentration.

TRUPATH assays

The allosteric activity for **368** was tested in combination with various orthosteric agonists (morphine, fentanyl and met-enkephalin) or antagonist (naloxone) on human μ OR and various mutants. To determine the negative allosteric effect of **368** on the coupling of the μ OR and the heterotrimeric G proteins, HEK293T cells were co-transfected in a 5:1:5:5 ratio of μ OR, individual G α -RLuc8 (G $_{\text{II}}$ or G $_{\text{I3}}$), G β $_3$ and GFP2-G γ $_8$ construct, whereas a combination of a 5:1:5:5 ratio of μ OR, individual G α -RLuc8 (G $_{\text{I2}}$, G $_{\text{O4}}$ or G $_{\text{O5}}$), G β $_3$ and GFP2-G γ $_8$ construct and a 5:1:5:5 ratio of μ OR, individual G α -RLuc8 (G $_{\text{I2}}$), G β $_3$ and GFP2-G γ $_1$ construct was used in the presence of transfection reagent (Transit 2020). The next day, the transfected cells were plated and incubated overnight into poly-L-lysine-coated 96-well white clear-bottom cell culture plates at a density of 50,000 cells per 200 μ l per well using DMEM supplemented with 1% dialysed fetal bovine serum. On the day after, cells were washed with 60 μ l of a drug buffer (1 \times HBSS and 20 mM HEPES, pH 7.4) per well after aspirating the medium. To measure the allosteric activity of **368** with individual orthosteric agonists, 60 μ l of 7.5 μ M RLuc substrate coelenterazine 400a (Nanolight) was added per well, followed by the addition of 30 μ l per well of 3 \times final concentrations (0 and 90 μ M) of **368** that was prepared in a drug buffer supplemented with 0.3% BSA and incubated for 20 min in the dark at room temperature. Finally, 30 μ l of 4 \times final various concentrations of morphine, fentanyl or met-enkephalin were prepared in a drug buffer containing 0.3% BSA then added and incubated for 5 min. To measure the allosteric activity of **368** with naloxone, 30 μ l of 2 \times final various concentrations of naloxone was added per well, followed by the addition of 30 μ l per well of 2 \times final concentrations (0 and 90 μ M) of **368** that was prepared in a drug buffer supplemented with 0.3% BSA and incubated for 20 min. Afterward, 60 μ l of 7.5 μ M RLuc substrate coelenterazine 400a (Nanolight) was loaded per well and incubated in the dark at room temperature. After 5 min, 30 μ l of 5 \times final concentration of DAMGO's EC $_{50}$ prepared in a drug buffer that contained 0.3% BSA was loaded per well and incubated in the dark at room temperature for an additional 5 min. Subsequently, a Mithras LB940 multimode microplate reader was used to measure the BRET ratios for G α protein activation by quantifying the ratio of the GFP2 emission to RLuc8 emission for 1 s per well at 510 nm and 395 nm, respectively. GraphPad Prism 9 software was used to determine the potency and E $_{\text{max}}$ of the examined orthosteric agonists and the antagonist by plotting their different used concentrations against BRET ratios that were normalized by defining 0% as basal and 100% as maximal values at 0 μ M concentration of **368** on wild-type μ OR.

Receptor cell surface expression

For the quantification of cell surface expression of wild-type μ OR and its mutants, an ELISA were performed. In brief, HEK293T cells were transfected with equivalent amounts of wild-type and mutant μ OR DNA and cultured for 24 h. Subsequently, the transfected cells were plated into poly-L-lysine-coated 96-well white clear-bottom plates at a density of 50,000 cells per 200 μ l per well using DMEM supplemented with 1% dialysed fetal bovine serum and the culture was maintained for an additional 24 h. The following day, cells were washed once with PBS (pH 7.4) and subsequently fixed with 4% (w/v) paraformaldehyde for 10 min at room temperature. After two washes with PBS, the cells were blocked with PBS containing 0.5% (w/v) BSA for 30 min at room temperature. Subsequently, the anti-Flag (M2)-horseradish peroxidase-conjugated antibody (Sigma-Aldrich) was added at a dilution of 1:20,000. After 1 h of incubation at room temperature, cells were washed 3 times and then incubated with 1-Step Ultra-TMB ELISA substrate (Thermo Fisher Scientific) at 37 °C for 15–30 min. Subsequently, the reaction was terminated with the addition of 1 M sulfuric acid and the absorbance at 450 nm was measured using a microplate reader (Biotek). The data are normalized with respect to the signal for wild-type μ OR, which is treated as 100%.

Formation and purification of μ OR– κ OR(ICL3)–naloxone–Nb6–**368** complex for cryo-EM studies

μ OR– κ OR(ICL3) was diluted to 20 μ M in 20 mM HEPES pH 7.5, 100 mM NaCl, 0.01% L-MNG, 0.003% GDN, 0.0013% CHS, 200 μ M naloxone and 200 μ M **368** and incubated for about 30 min followed by addition of 2:1 molar excess of Nb6 and further incubation on ice overnight. Excess Nb6 was removed by M1 anti-Flag immunoaffinity chromatography, and the pure μ OR– κ OR(ICL3)–Nb6–naloxone–**368** complex was eluted in a buffer composed of 20 mM HEPES pH 7.5, 100 mM NaCl, 0.00075% L-MNG, 0.00025% GDN, 0.0001% CHS, 100 μ M naloxone, 100 μ M **368**, Flag peptides and 5 mM EDTA. The complex was concentrated to about 16 mg ml $^{-1}$ for EM and analysis by SDS-PAGE.

Cryo-EM data acquisition and processing

μ OR– κ OR(ICL3)–naloxone–Nb6–368**.** The μ OR– κ OR(ICL3)–naloxone–Nb6–**368** complex was applied to glow-discharged 200 mesh grids (UltrAuFoil R1.2/1.3) at a concentration of about 16 mg ml $^{-1}$ and vitrified using a Vitrobot Mark IV (Thermo Fisher Scientific) at 100% humidity at 22 °C after blotting for 3 s with a blot force of 3. Cryo-EM images were collected on a Titan Krios (Thermo Fisher Scientific) equipped with X-FEG and Selectis X image filter operated at 300 kV at a nominal magnification of \times 165,000 using a Falcon 4 camera in counting mode corresponding to a pixel size of 0.741 Å. A total of 10,007 image stacks were obtained with a dose rate of 5.0 e $^{-}$ per pixel per s and total exposure time of 6.6 s, resulting in a total dose of 60 electrons per Å 2 . The defocus range was set to –0.6 to –1.4 μm.

Dose-fractionated image stacks were imported to Relion⁵⁰ and subjected to patch-based beam-induced motion correction using MotionCor2 (ref. 51) and CTF parameters were determined with CTFFIND4 (ref. 52). After removing micrographs with an estimated CTF resolution of less than 3.4 Å, a total of 4,254,557 particles were picked using a template-based autopicking protocol. These particles were imported to CryoSPARC⁵³ for several rounds of 2D classification, resulting in 898,414 particles. These particles were then subjected to iterative rounds of 3D classification using ab initio classification with concurrent 2D classification rounds to rescue particles from bad 3D classes. After a final round of 2D classification, a set of 128,613 final particles were reconstructed to 3.26 Å nominal resolution at FSC value of 0.143 with local refinement. Local resolution was estimated using CryoSPARC⁵³.

Model building and refinement. The initial template for the μ OR– κ OR(ICL3)–naloxone–Nb6–**368** structure was derived from the μ OR– κ OR(ICL3)–alvimopan–Nb6 structure solved previously²⁹. The initial model was docked into the EM density map using UCSF Chimera followed by iterative model building in Coot⁵⁴. Ligand coordinates (naloxone, **368**) and geometry restraints were initially generated using phenix.elbow⁵⁵. The final model was subjected to global refinement and minimization in real space with phenix.real_space_refine⁵⁶. Residues with weak side chain density were stubbed while preserving sequence information. Molprobity⁵⁷ was used to evaluate model geometry. The final pose for **368** was evaluated with all-atom molecular dynamics simulations (described below) and compared with other potential poses. The final refinement parameters are provided in Extended Data Table 3 for μ OR– κ OR(ICL3)–naloxone–Nb6–**368**.

Molecular dynamics simulations

System set-up. Simulation systems were built using CHARMM-GUI⁵⁸ with Membrane Builder^{59–62}. The chains for the receptor and ligands from the structure presented here (naloxone and **368** for the μ OR– κ OR(ICL3)–naloxone–Nb6–**368** complex) were selected, and other proteins (for example, Nb6) were removed. CHARMM General Force Field^{63,64} was used to generate topology and parameter files for the small-molecule ligands (**368** and naloxone). Missing side chains were modelled in CHARMM-GUI, and the receptor chains were capped

Article

with neutral N-terminal acetyl groups and C-terminal methylamide groups. Titratable groups were simulated in their dominant protonation state for pH 7. The receptors were placed in the membrane by aligning the first principal axis of the receptor to the z axis, followed by visual inspection. The aligned structures were then inserted into a palmitoyl-oleoyl-phosphatidylcholine (POPC) bilayer with a minimum water height on either side of the bilayer of 22.5 Å and a bilayer area chosen to be about 4 times that of the protein surface, normalizing the upper and lower leaflet surface area by additional POPC molecules accordingly. KCl (150 mM) ions were added to neutralize the system charge.

Simulation protocol. All simulations were performed using CHARMM36m force field⁶⁵ for proteins, ions and lipids, and TIP3 model⁶⁶ was used for waters. Simulations were performed using OpenMM⁶⁷ on single graphics processing units. The system was equilibrated initially with 1 fs time steps (125 ps per run for 3 runs) followed by 2 fs time steps (500 ps per run for 3 runs) for a total of 6 equilibration steps each with continually decreasing force constants applied to the protein backbone (10.0, 5.0, 2.5, 1.0, 0.5, 0.1 kcal mol⁻¹ Å⁻²), side chains (5.0, 2.5, 1.0, 0.5, 0.1, 0.0 kcal mol⁻¹ Å⁻²), waters and lipids (2.5, 2.5, 1.0, 0.5, 0.1, 0.0 kcal mol⁻¹ Å⁻²) and ions (10.0, 0.0, 0.0, 0.0, 0.0, 0.0 kcal mol⁻¹ Å⁻²). Production runs were performed in NPT ensemble at 310.15 °K at 1 bar with 4 fs time steps using hydrogen mass repartitioning⁶⁸. Bonds to hydrogen atoms were constrained with the SHAKE algorithm⁶⁹. A switching distance of 10 Å and cut-off distance of 12 Å were used for nonbonded interactions, and long-range electrostatics were computed with particle mesh Ewald. Coordinates were written out every 100 ps. Ligand and Cα r.m.s.d. values were calculated throughout the trajectories after rigid body alignment to the receptor backbone Cα using MDAnalysis^{70,71}.

In vivo experiments

All experiments used male C57BL/6J mice (Jackson Laboratory; 20–35 g) between 8 and 13 weeks old at 5 per cage with a 12-h light–dark cycle (that is, lights off at 19:00 and on at 7:00) with ad libitum access to food and water. Mice were kept at a constant temperature (20–24 °C) and relative humidity (40–50%). All studies reported here are in compliance with ARRIVE guidelines⁷² and the National Institutes of Health guide for care and use of animals (NIH publication no. 8023, revised 1978) and were approved and conducted in agreement with the Institutional Animal Care and Use Committees at the University of Florida. Mice were used in pharmacokinetics¹², warm-water tail withdrawal^{73,74}, locomotor and respiration (through CLAMS assays)^{73,74}, CPP^{73,75} and naloxone-precipitated opioid withdrawal assays³⁹, all described in detail below.

Compound treatment. **368** (racemic mixture) was synthesized as described above. Other drugs (morphine, fentanyl and naloxone) were purchased and used as previously described^{12,39}.

Pharmacokinetics of **368.** **368** was administered to mice intravenously at 10 mg kg⁻¹ dose in *n* = 4 C57BL/6J mice for each time point. After 30, 60 or 120 min, mice were anaesthetized with isoflurane followed by removal of blood and the animals were killed for removal of the brain. Brains were rinsed with PBS, dried, flash-frozen and weighed for subsequent studies of brain penetration of **368**. Tissue samples were placed into Navy bead lysis kit tubes and compared against naïve tissue, which was used for standard, quality control and blank samples. An appropriate volume of cold acetonitrile:water (3:1) was added to each sample tube to normalize the concentrations to 250 mg ml⁻¹. Tubes were then placed into a bead heater for 3 min, followed by centrifugation at 3,200 r.p.m. for 5 min at 4 °C. The resulting supernatants were transferred to Eppendorf tubes and stored at –80 °C until analysis.

For analysis, samples were thawed on ice and extensively mixed, followed by further centrifugation at 3,200 r.p.m. for 5 min at 4 °C.

A volume of 30 µl of supernatant was collected and transferred to a 96-well plate along with 30 µl standards, quality controls, blanks and double blanks. Cold acetonitrile (150 µl) spiked with internal standard was then added to blanks, standards, quality controls and unknown samples, whereas cold acetonitrile alone was added to double blanks. Samples were mixed for 10 min followed by further centrifugation at 3,200 r.p.m. for 10 min at 4 °C. Supernatants after centrifugation were evaporated to dryness in a 96-well plate, followed by reconstitution with 100 µl 0.1% v/v formic acid in water:acetonitrile (90:10). The plate was sealed, vortexed and briefly centrifuged to settle the samples, and was submitted for LC–MS analysis as previously described^{12,37} using a mass spectrometer (SCIEX Triple Quad 5500+ system–QTRAP ready) linked to a liquid chromatography system (ExionLC AD–HPLC).

Antinociceptive testing. The 55 °C warm-water tail-withdrawal assay was performed as previously described^{38,76}. Latency of the mouse to remove its tail from warm water was recorded as the end point. After determining baseline tail-withdrawal latencies, mice were administered opioid agonists with or without s.c. pretreatment with vehicle (10% DMSO/10% solutol/80% saline, 0.9%), a graded dose of **368** (1–100 mg kg⁻¹) and/or naloxone (*n* = 8–14 per group). Vehicle or **368** was administered 30 min before administering saline or naloxone (0.1, 1 or 10 mg kg⁻¹) 15 min before morphine (10 mg kg⁻¹, s.c.), at which point the tail-withdrawal assay was performed every 10 min until return to baseline responses were achieved (up to 150 min). To avoid excess tissue damage, mice that failed to withdraw their tails after 15 s had their tails removed from the bath and were assigned a maximum antinociceptive response (100%, see below equation). The assay was additionally performed with fentanyl as the orthosteric opioid agonist, but fentanyl was administered at 0.1 mg kg⁻¹. At each time point, antinociception was then calculated as follows:

$$\text{Antinociception (\%)} = 100 \times ((\text{test latency} - \text{baseline latency}) / (15 - \text{baseline latency}))$$

As shown in Fig. 4a, low-dose naloxone had no significant effect on morphine-induced antinociception ($F_{(12,168)} = 0.49, P = 0.92$; two-way repeated measures (RM) ANOVA), whereas increasing concentrations of **368** in the presence of low-dose naloxone significantly inhibited morphine-induced antinociception ($F_{(4,35)} = 50.1, P < 0.0001$; two-way RM ANOVA). As shown in Fig. 4d, 0.5 mg kg⁻¹ naloxone was not able to significantly reverse 0.1 mg kg⁻¹ fentanyl-induced antinociception ($F_{(7,98)} = 2.090, P = 0.052$), whereas addition of 100 mg kg⁻¹ **368** caused a significant enhancement in the ability of naloxone to reverse fentanyl-induced antinociception ($F_{(7,98)} = 6.382, P < 0.0001$). Data are displayed as the average percentage antinociception ± s.e.m. of *n* = 8–14 mice for both Fig. 4a and Fig. 4d.

Locomotor and respiration effects. Locomotor activity (as ambulations) and respiratory depression (as breaths per min) were measured using automated, closed-air CLAMS in a similar manner to that previously described^{38,39,77}. In brief, mice were habituated in chambers for 60 min, during which baselines for each animal were measured. Vehicle or increasing doses of **368** (1–100 mg kg⁻¹) was then administered, followed 30 min later by administration of vehicle, morphine (10 mg kg⁻¹) or morphine with low-dose naloxone (0.1 mg kg⁻¹), and confined 5 min later in individual CLAMS testing chambers for measurements lasting 200 min. The respiration rate (breaths per min) was measured using pressure transducers built into the sealed CLAMS cages, whereas infrared beams located in the cage floors measured ambulations through sequential beam breaks. Data are expressed as percentages of vehicle responses ± s.e.m. (for *n* = 11–16 mice per group) for ambulations or breaths per min, averaged over 20-min periods for 140 min after injection of the test compound.

As shown in Fig. 4b,c, morphine caused significant increases in locomotion ($F_{(6,108)} = 54.7, P < 0.0001$; two-way RM ANOVA with Sidak post hoc test) and significant decreases in breathing rate ($F_{(6,108)} = 4.09, P = 0.001$; two-way RM ANOVA). Low-dose naloxone did not significantly affect hyperlocomotion ($F_{(1,18)} = 0.62, P = 0.44$; two-way RM ANOVA) and only modestly inhibited respiratory depression ($F_{(1,18)} = 11.7, P = 0.003$; two-way RM ANOVA). A dose of 100 mg kg^{-1} **368** alone did not significantly affect locomotion ($F_{(6,108)} = 0.36, P = 0.90$; two-way RM ANOVA) or respiratory depression ($F_{(6,108)} = 1.19, P = 0.32$; two-way RM ANOVA). It did, however, cause significant enhancements in the ability of low-doses of naloxone to reverse both hyperlocomotion ($F_{(24,306)} = 4.27, P < 0.0001$; two-way RM ANOVA with Tukey post hoc test) and respiratory depression ($F_{(24,294)} = 5.00, P < 0.0001$; two-way RM ANOVA with Tukey post hoc test). Data are displayed in Fig. 4b,c as 20-min bins as percentages relative to vehicle responses \pm s.e.m. for $n = 11$ or 16 mice in Fig. 4c and Fig. 4b, respectively, for cohorts with low-dose naloxone and $n = 8$ morphine alone or with **368**.

CPP assay. Groups of mice ($n = 18$ – 26 per group) were place-conditioned using a counterbalanced design in a three-chamber place-conditioning system (San Diego Instruments) as previously described^{37,73}. The amount of time individual mice spent in each compartment both before and after place conditioning was measured over a 30-min testing period, during which animals freely explored the three compartments. Following determination of initial preference, mice were administered 0.9% saline, and half the sample consistently confined in a randomly assigned outer chamber for 40 min. Four hours later, mice were pretreated s.c. for 30 min with either vehicle or **368** (100 mg kg^{-1}), followed by all mice receiving low-dose naloxone (0.1 mg kg^{-1} , s.c.). Fifteen minutes later, mice were administered morphine (10 mg kg^{-1} , i.p.) and place conditioned for 40 min in the opposite outer chamber. Mice were place conditioned in this manner for 2 days, with a final place preference performed on the fourth day. Data are plotted as the difference in time spent in the eventual morphine-paired chamber versus the vehicle-paired compartment.

In Fig. 4e, morphine alone produced significant CPP (left blue bars, $F_{(2,64)} = 6.65, P = 0.002$, $n = 18$ mice; two-way RM ANOVA with Tukey's post hoc test) that was not inhibited by 0.1 mg kg^{-1} naloxone (central bars, $n = 26$ mice, $P = 0.009$; Tukey's post hoc test). However, treating with 0.1 mg kg^{-1} naloxone and 100 mg kg^{-1} **368** resulted in an elimination of morphine-induced CPP (right purple bars; $n = 23$ mice; $P = 0.09$; Tukey's post hoc test). Data are displayed as the average difference in time spent in morphine-paired chambers \pm s.e.m.

Naloxone-precipitated opioid withdrawal assay. Mice were made physically dependent on morphine using previously established methods^{38,39}. In brief, mice were placed into four groups ($n = 10$ – 11 per group) and were given either saline (group 1) or escalating doses of morphine (10 – 75 mg kg^{-1} , groups 2–4) twice daily for 4 days. A final dose of saline (for group 1) or morphine (25 mg kg^{-1}) was given on day 5 to assess antinociceptive tolerance. Two hours later, precipitated withdrawal symptoms were assessed for 15 min following various treatments. Groups 1 and 2 were given a conventional dose of naloxone (10 mg kg^{-1}), whereas groups 3 and 4 were pretreated 30 min with either saline (3) or **368** ($4, 100 \text{ mg kg}^{-1}$, s.c.) ahead of administration of low-dose naloxone (0.1 mg kg^{-1}). Immediately after the various naloxone treatments, withdrawal behaviours were quantified from mice in $16 \times 45 \text{ cm}$ Plexiglass cylinders for 15 min following established protocols^{38,39}.

As shown in Fig. 4f, **368** with low doses of naloxone increased the teeth chattering frequency, although not to the same extent as full doses of naloxone alone ($F_{(3,37)} = 12.8, P < 0.0001$; one-way ANOVA with Tukey post hoc test). As shown in Fig. 4g, low doses (0.1 mg kg^{-1}) of naloxone significantly increased the jumping frequency on its own ($F_{(3,37)} = 17.0, P < 0.0001$; one-way ANOVA), although this effect was not enhanced by **368** ($P = 0.66$, Tukey post hoc test). As shown in Fig. 4h,

both low and high doses of naloxone caused significant diarrhoea in mice ($F_{(3,37)} = 23.8, P < 0.0001$; one-way ANOVA with Tukey post hoc test), whereas **368** inhibited diarrhoea such that there was no significant difference from saline control ($P = 0.61$; Tukey's post hoc test). Data are displayed for Fig. 4f–h as the mean value of $n = 10$ mice ($n = 11$ for condition 2).

Figure preparation

Protein structure figures were created using the PyMOL Molecular Graphics System (v.2.3.5 Schrödinger; <http://pymol.org>). Density map figures were created using UCSF Chimera⁷⁸ and UCSF Chimera X⁷⁹. Graphs were created using GraphPad Prism. The schematic in Fig. 1 was created using BioRender (<https://biorender.com>). Molecular dynamics trajectories were analysed using MDAnalysis^{70,71}. Figures were constructed in Adobe Illustrator.

Reporting summary

Further information on research design is available in the Nature Portfolio Reporting Summary linked to this article.

Data availability

All data supporting the findings of this study are available within the article, extended data, Supplementary Information or the associated data tables. Original raw data will be provided upon request for all experiments, including supporting information. The cryo-EM density map has been deposited into the Electron Microscopy Data Bank under accession code EMD-44635. Model coordinates have been deposited into the PDB under accession number 9BJK. Source data are provided with this paper.

Code availability

This manuscript does not report any new code.

48. Kumar, K. K. et al. Structure of a signaling cannabinoid receptor 1-G protein complex. *Cell* <https://doi.org/10.1016/j.cell.2018.11.040> (2019).
49. Wang, H. et al. Structure-based evolution of G protein-biased μ -opioid receptor agonists. *Angew. Chem. Int. Ed.* <https://doi.org/10.1002/anie.202200269> (2022).
50. Zivanov, J. et al. New tools for automated high-resolution cryo-EM structure determination in RELION-3. *eLife* **7**, e42166 (2018).
51. Zheng, S. Q. et al. MotionCor2: anisotropic correction of beam-induced motion for improved cryo-electron microscopy. *Nat. Methods* **14**, 331–332 (2017).
52. Rohou, A. & Grigorieff, N. CTFFIND4: fast and accurate defocus estimation from electron micrographs. *J. Struct. Biol.* **192**, 216–221 (2015).
53. Punjani, A., Rubinstein, J. L., Fleet, D. J. & Brubaker, M. A. CryoSPARC: algorithms for rapid unsupervised cryo-EM structure determination. *Nat. Methods* **14**, 290–296 (2017).
54. Emsley, P. & Cowtan, K. Coot: model-building tools for molecular graphics. *Acta Crystallogr. D Biol. Crystallogr.* **60**, 2126–2132 (2004).
55. Moriarty, N. W., Grosse-Kunstleve, R. W. & Adams, P. D. Electronic ligand builder and optimization workbench (eLBOW): a tool for ligand coordinate and restraint generation. *Acta Crystallogr. D Biol. Crystallogr.* **65**, 1074–1080 (2009).
56. Adams, P. D. et al. The Phenix software for automated determination of macromolecular structures. *Methods* **55**, 94–106 (2011).
57. Williams, C. J. et al. MolProbity: more and better reference data for improved all-atom structure validation. *Protein Sci.* **27**, 293–315 (2018).
58. Jo, S., Kim, T., Iyer, V. G. & Im, W. CHARMM-GUI: a web-based graphical user interface for CHARMM. *J. Comput. Chem.* **29**, 1859–1865 (2008).
59. Wu, E. L. et al. CHARMM-GUI Membrane Builder toward realistic biological membrane simulations. *J. Comput. Chem.* **35**, 1997–2004 (2014).
60. Jo, S., Lim, J. B., Klauda, J. B. & Im, W. CHARMM-GUI Membrane Builder for mixed bilayers and its application to yeast membranes. *Biophys. J.* **97**, 50–58 (2009).
61. Jo, S., Kim, T. & Im, W. Automated builder and database of protein/membrane complexes for molecular dynamics simulations. *PLoS ONE* **2**, e880 (2007).
62. Lee, J. et al. CHARMM-GUI Membrane Builder for complex biological membrane simulations with glycolipids and lipoglycans. *J. Chem. Theory Comput.* **15**, 775–786 (2019).
63. Yu, W., He, X., Vanommeslaeghe, K. & Mackerell, A. D. Jr. Extension of the CHARMM general force field to sulfonyl-containing compounds and its utility in biomolecular simulations. *J. Comput. Chem.* **33**, 2451–2468 (2012).
64. Vanommeslaeghe, K. et al. CHARMM general force field: a force field for drug-like molecules compatible with the CHARMM all-atom additive biological force fields. *J. Comput. Chem.* **31**, 671–690 (2009).
65. Huang, J. et al. CHARMM36m: an improved force field for folded and intrinsically disordered proteins. *Nat. Methods* **14**, 71–73 (2017).

Article

66. Jorgensen, W. L., Chandrasekhar, J., Madura, J. D., Impey, R. W. & Klein, M. L. Comparison of simple potential functions for simulating liquid water. *J. Chem. Phys.* **79**, 926–935 (1983).
67. Eastman, P. et al. OpenMM 7: rapid development of high performance algorithms for molecular dynamics. *PLoS Comput. Biol.* **13**, e1005659 (2017).
68. Hopkins, C. W., Le Grand, S., Walker, R. C. & Roitberg, A. E. Long-time-step molecular dynamics through hydrogen mass repartitioning. *J. Chem. Theory Comput.* **11**, 1864–1874 (2015).
69. Ryckaert, J.-P., Ciccotti, G. & Berendsen, H. J. C. Numerical integration of the cartesian equations of motion of a system with constraints: molecular dynamics of *n*-alkanes. *J. Comput. Phys.* **23**, 327–341 (1977).
70. Michaud-Agrawal, N., Denning, E. J., Woolf, T. B. & Beckstein, O. MDAnalysis: a toolkit for the analysis of molecular dynamics simulations. *J. Comput. Chem.* **32**, 2319–2327 (2011).
71. Gowers, R. J. et al. MDAnalysis: a Python package for the rapid analysis of molecular dynamics simulations. In *Proc. 15th Python in Science Conference* (eds Bentham, S. & Rostrup, S.) 98–105 (SciPy, 2016).
72. Kilkenny, C., Browne, W. J., Cuthill, I. C., Emerson, M. & Altman, D. G. Improving bioscience research reporting: the ARRIVE guidelines for reporting animal research. *Animals* **4**, 35–44 (2014).
73. Chakraborty, S. et al. A novel mitragynine analog with low-efficacy mu opioid receptor agonism displays antinociception with attenuated adverse effects. *J. Med. Chem.* **64**, 13873–13892 (2021).
74. Wilson, L. L. et al. Characterization of CM-398, a novel selective sigma-2 receptor ligand, as a potential therapeutic for neuropathic pain. *Molecules* **27**, 3617 (2022).
75. Upadhyay, R. et al. Controlling opioid receptor functional selectivity by targeting distinct subpockets of the orthosteric site. *eLife* **10**, e56519 (2021).
76. Reiley, K. J. et al. Identification of two novel, potent, low-liability antinociceptive compounds from the direct *in vivo* screening of a large mixture-based combinatorial library. *AAPS J.* **12**, 318–329 (2010).
77. Brice-Tutt, A. C. et al. Multifunctional opioid receptor agonism and antagonism by a novel macrocyclic tetrapeptide prevents reinstatement of morphine-seeking behaviour. *Br. J. Pharmacol.* **177**, 4209–4222 (2020).
78. Pettersen, E. F. et al. UCSF Chimera—a visualization system for exploratory research and analysis. *J. Comput. Chem.* **25**, 1605–1612 (2004).
79. Pettersen, E. F. et al. UCSF ChimeraX: structure visualization for researchers, educators, and developers. *Protein Sci.* **30**, 70–82 (2021).

Acknowledgements We thank staff at WuXi AppTec for providing the DEL and off-DNA synthesis of hits; J.Su for providing structure–activity relationship information for chemical families; and M. Robertson for providing the μ OR κ and Nb6 vectors. Cryo-EM data were collected at S2C2. K.K.K. was supported by the American Diabetes Association (ADA) Postdoctoral Fellowship. E.S.O. was supported by the American Heart Association (AHA) Postdoctoral Fellowship. S.M. and J.P.M. are supported by RO1DA057790. B.K.K. was supported by the Chan Zuckerberg Biohub and by RO1DA036246.

Author contributions E.S.O., V.A.R., S.M., J.P.M. and B.K.K. wrote the manuscript with input from all authors. E.S.O., W.H., K.K. and B.K.K. designed the DEL screening strategy. E.S.O. performed DEL selections. E.W. and E.S.O. designed, optimized and performed the radioligand-binding experiments. E.S.O., W.H. and Y.S. optimized and performed the GTP turnover assays. J.M.M. performed the *in-cell* cAMP experiments. E.S.O. formed the complexes for the cryo-EM studies, collected and processed cryo-EM data with assistance from H.W. and C.Z., built the structural models with assistance from K.K., and performed and analysed the molecular dynamics simulations. V.A.R. synthesized (\pm)-**368**, its pure enantiomers, developed a scale-up synthesis of (\pm)-**368** and chemical characterization under S.M.’s supervision. K.A. carried out pharmacokinetics analysis of (\pm)-**368** under S.M.’s supervision. A.E. and Q.J. performed TRUPATH experiments with supervision from T.C. S.O.E., H.R.H. and J.P.M. performed and analysed all behavioural pharmacology experiments. B.J.K. developed and performed the chiral analysis.

Competing interests B.K.K. is a founder and consultant for ConformetRx. S.M. is a founder of Sparian Biosciences. E.S.O., K.K.K., V.A.R., S.M. and B.K.K. have filed a patent around the new NAM compound acting through μ OR. B.J.K. is an employee of Lotus Separations. The remaining authors declare no other competing interests.

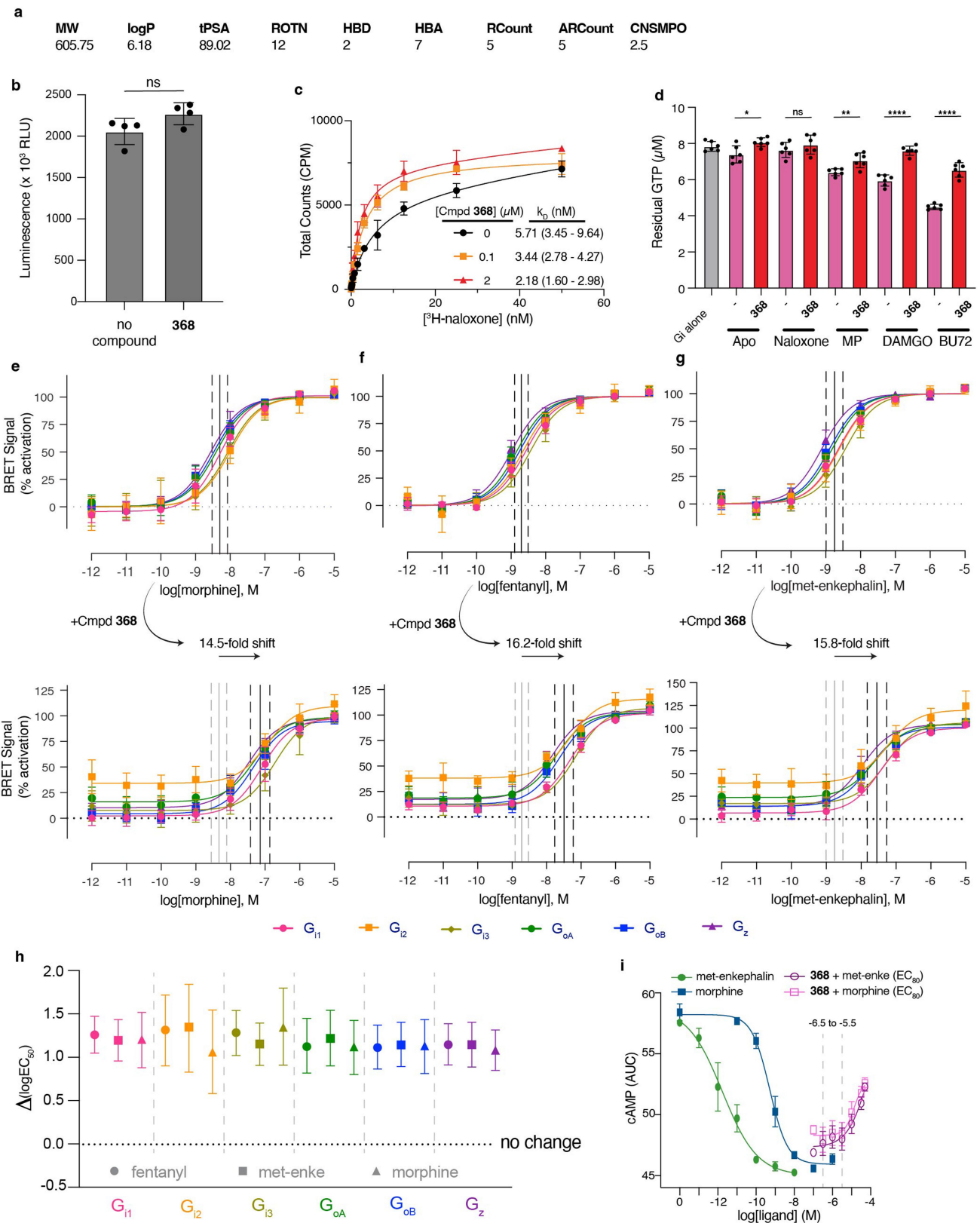
Additional information

Supplementary information The online version contains supplementary material available at <https://doi.org/10.1038/s41586-024-07587-7>.

Correspondence and requests for materials should be addressed to Jay P. McLaughlin, Susrita Majumdar or Brian K. Kobilka.

Peer review information *Nature* thanks Catherine Cahill and the other, anonymous, reviewer(s) for their contribution to the peer review of this work.

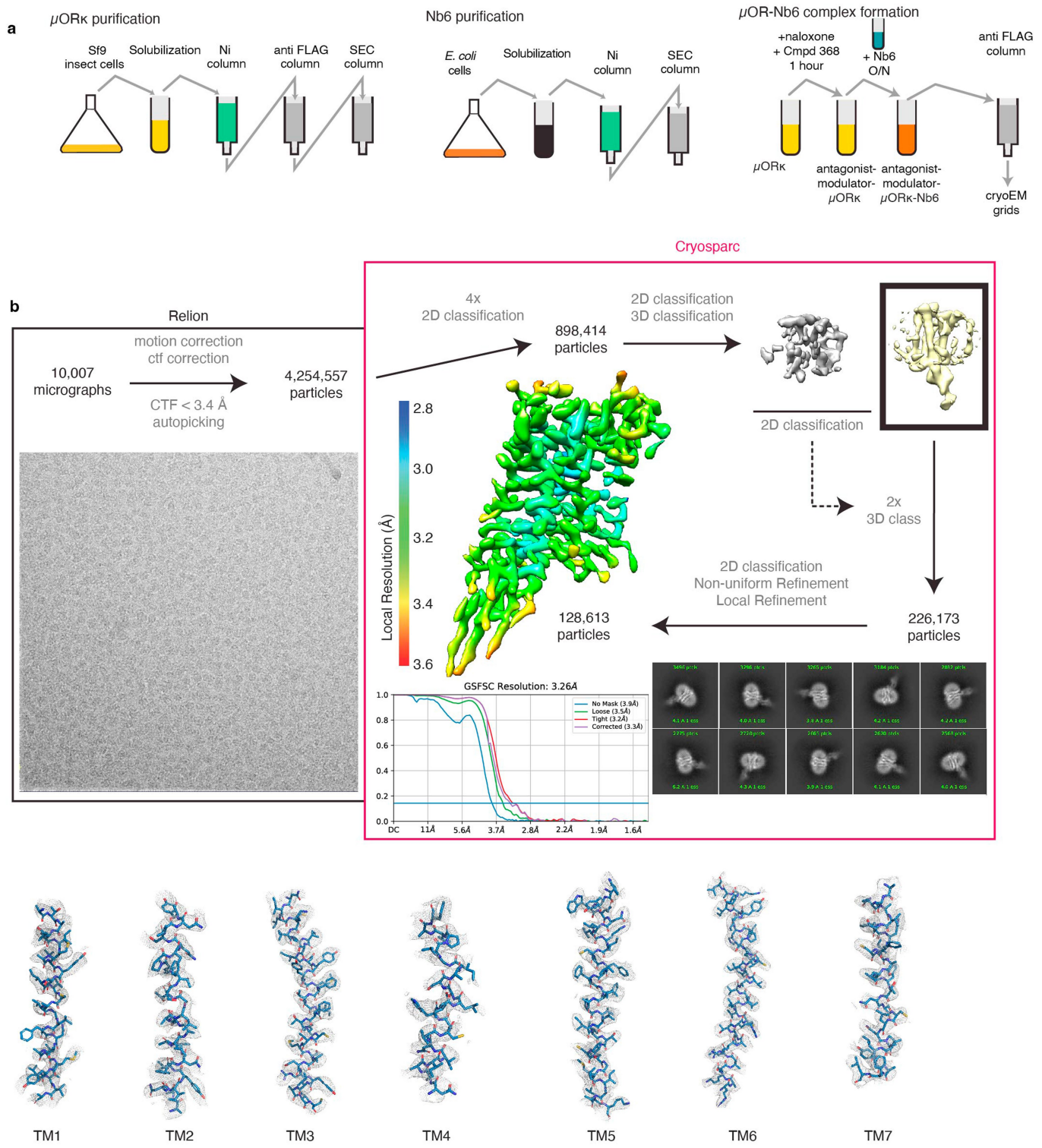
Reprints and permissions information is available at <http://www.nature.com/reprints>.



Extended Data Fig. 1 | See next page for caption.

Article

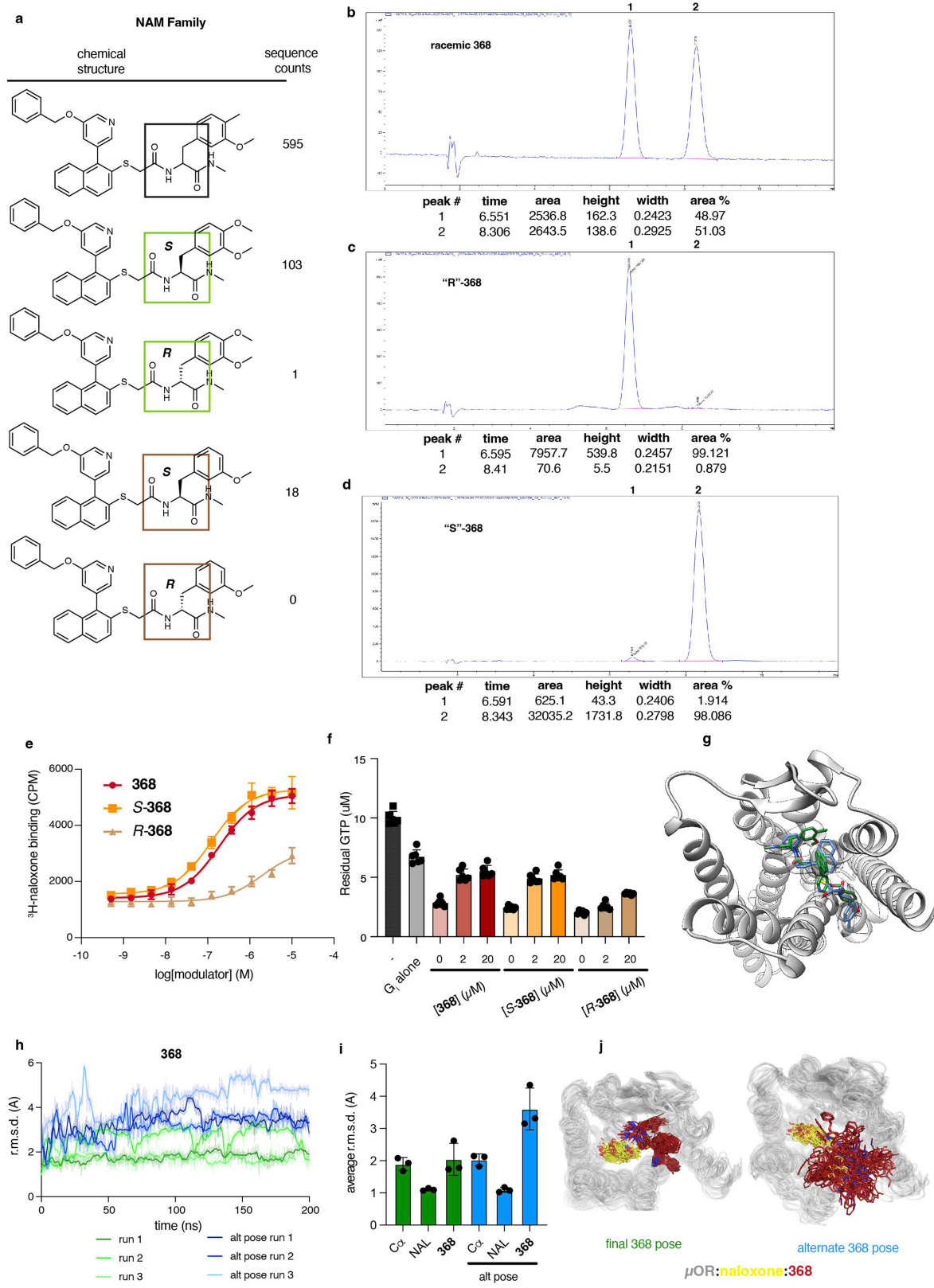
Extended Data Fig. 1 | Initial biochemical characterization of μOR allosteric modulators from DEL screen. (a) Chemical properties of **368**. MW; molecular weight (Da). logP; predicted octanol/water partition coefficient. PSA; polar surface area (Å²). ROTN; rotatable bonds. HBD; hydrogen bond donors. HBA; hydrogen bond acceptors. RCount; number of rings. ARCount; number of aromatics. CNSMPO; central nervous system multiparameter optimization. LogP was predicted using QikProp in Schrödinger, and other properties were calculated using ChemDraw. (b) Excess concentrations of **368** have no impact ($P = 0.084$) on G_{i1} intrinsic turnover in the absence of receptor. Data are displayed as the average \pm s.d. with $n = 4$ individual experiments. (c) We show using a direct ³H-naloxone binding experiment that increasing concentrations of **368** result in an increased antagonist affinity for μOR-containing membranes. Fitted affinity values are shown along with 95% confidence intervals in parentheses. Data are displayed as average values with error bars corresponding to the standard deviations of $n = 4$ measurements (d) The GTP turnover assay was used to show that 20 μM **368** inhibits turnover for a wide variety of orthosteric site conditions, ranging from slight inhibition of basal signaling ($P = 0.015$) to no detectable effect on naloxone turnover ($P = 0.314$) to substantial inhibition of moderate partial agonist turnover (mitragynine pseudoindoxyl, MP, $P = 0.005$) to peptide (DAMGO, $P < 0.0001$) or small molecule (BU72, $P < 0.0001$) full agonists (all orthosteric molecules also present at 20 μM, data are displayed as the average \pm s.d. with $n = 4$ individual experiments). P values for all of the above were calculated using an unpaired t-test (two tailed) and are denoted as follows: ns ($P > 0.05$), * ($P \leq 0.05$), ** ($P \leq 0.01$), *** ($P \leq 0.001$), and **** ($P \leq 0.0001$). Titrations of (e) morphine, (f) fentanyl, and (g) met-enkephalin result in activation of an assortment of G-proteins (G_{i1} , pink; G_{i2} , orange; G_{i3} , pale green; G_{oA} , green; G_{oB} , blue; and G_z , purple) as observed in the TRUPATH assay by a change in BRET signal as the $G\alpha$ and $G\beta$ subunits separate. Activation by all 3 agonists was also calculated in the presence of 90 μM **368** (bottom panels). The data are displayed as the average \pm s.d. with $n = 6$ individual experiments. The average log(EC₅₀) for all 6 G-protein activation curves within each panel is shown as a black line (with dashed grey lines representing the standard deviation among different G protein subtypes). The average fold change in EC₅₀ upon addition of **368** for morphine (14.5), fentanyl (16.2) and met-enkephalin (15.8) is shown. (h) The presence of excess (90 μM) **368** results in decreased agonist potencies for a variety of orthosteric agonists (fentanyl, circles; met-enkephalin, squares; morphine, triangles) across a series of $G_{i/o}$ family G-protein effectors as observed by the TRUPATH assay for G-protein activation. The calculated log(EC₅₀) for all agonist/G-protein combinations are right-shifted by -1-1.5 units in the presence of **368**. Data are displayed as average changes in log(EC₅₀ values) for each condition with error bars corresponding to the additive fitted error 95% confidence intervals for EC₅₀ values with and without **368**. (i) This $G_{i/o}$ family inhibition results in dampened cAMP inhibition in cells with morphine (dark blue vs. pink) and met-enkephalin (green vs. purple). Titration of **368** at EC₅₀ concentrations of orthosteric agonists results in the reversal of cAMP inhibition, though with weaker potencies than those observed biochemically. Data are displayed as the average \pm s.d. with $n = 5$ individual experiments.



Extended Data Fig. 2 | CryoEM structure determination of μORk-Nb6 bound to naloxone and 368. (a) Schematic of μORk purification and complex formation with Nb6. (b) Cryo-EM data collection and processing pipeline, showing representative micrographs of the μORk-Nb6 complex, reference-free 2D cryo-EM class averages, and processing flow chart. This includes motion

and CTF correction in Relion, followed by particle selection, 2D and 3D classifications, density map reconstructions, “gold standard” FSC curves in Cryosparc, and the final density map colored by local resolution. Also included is the cryo-EM density map and model for the seven transmembrane helices of the μORk.

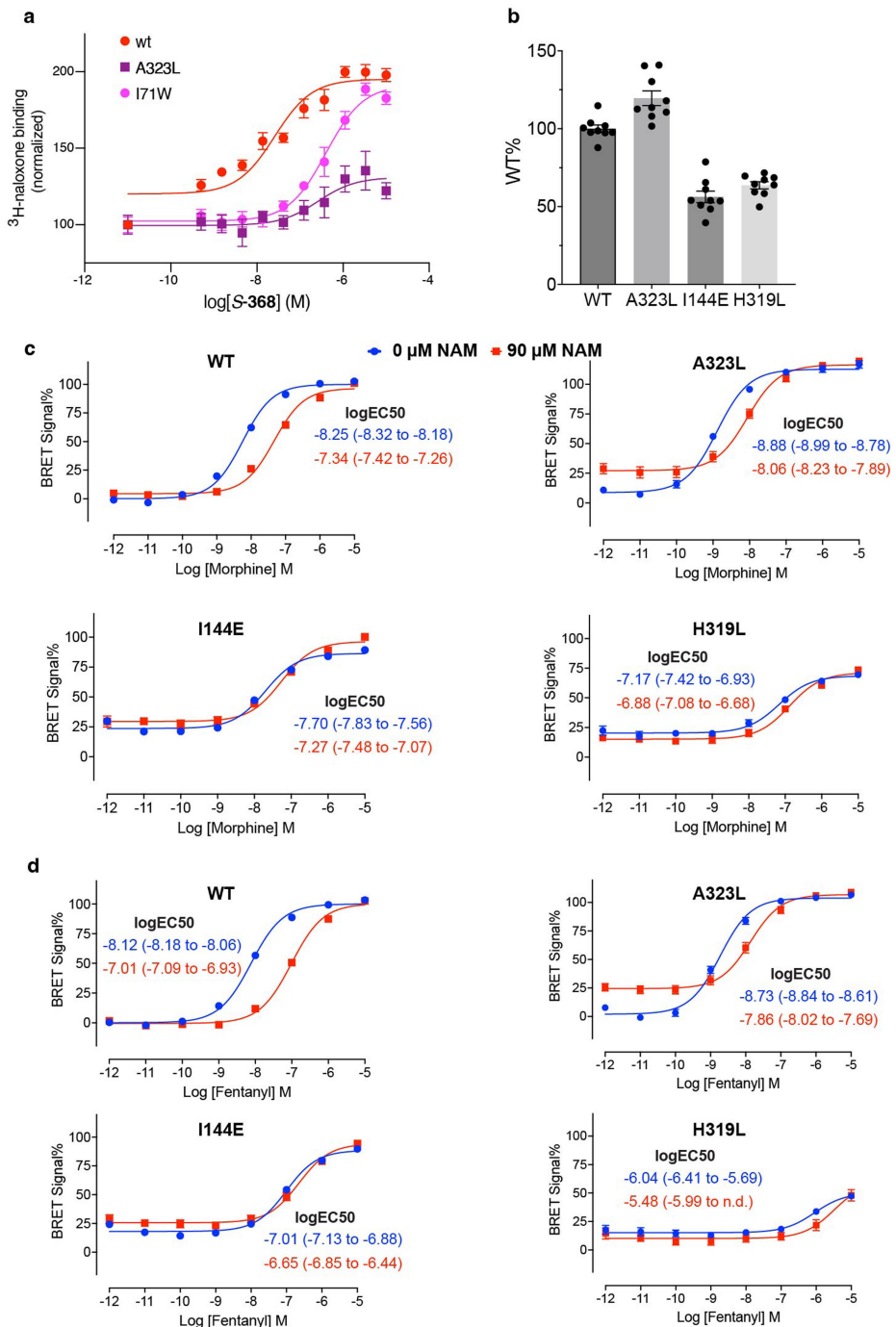
Article



Extended Data Fig. 3 | See next page for caption.

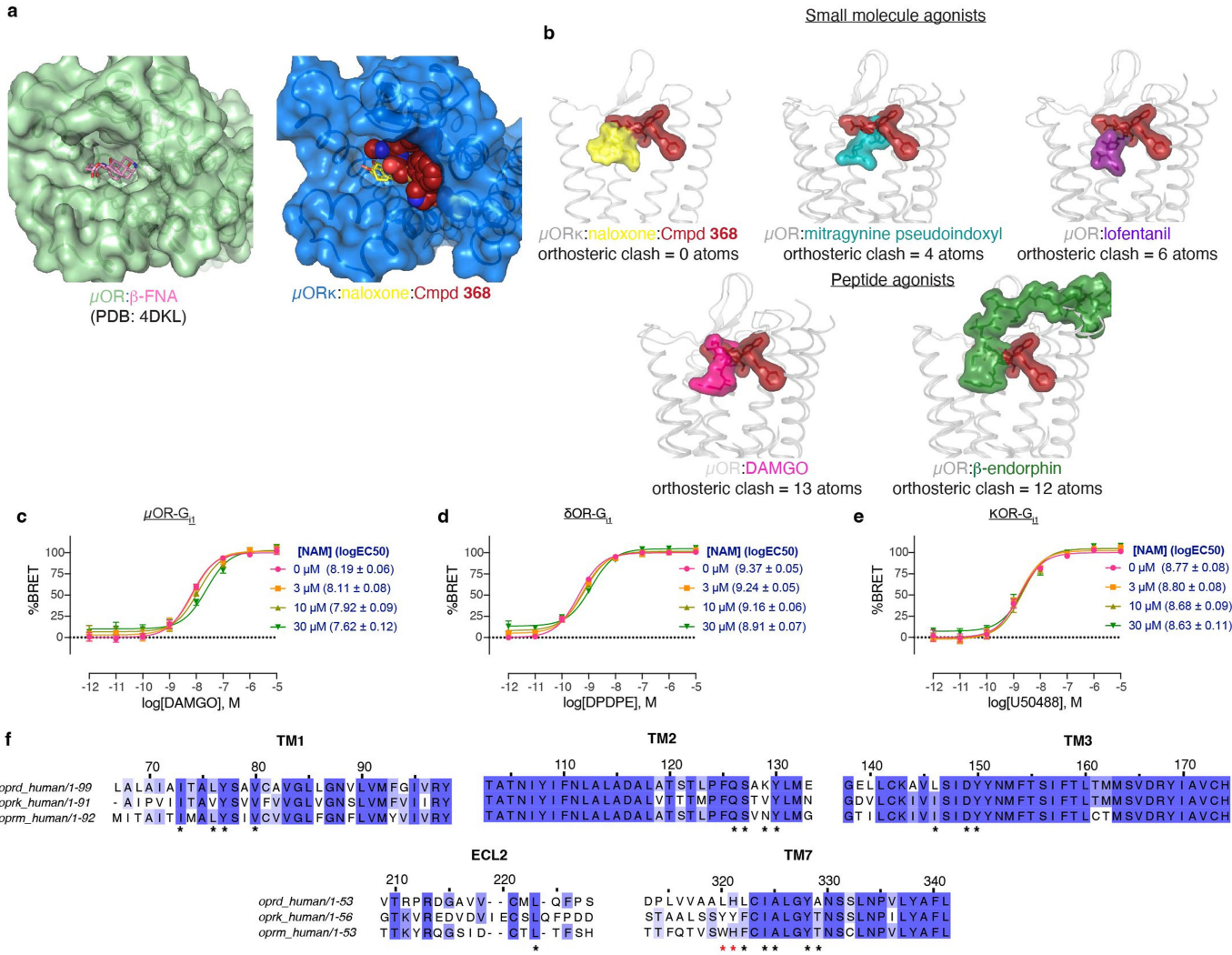
Extended Data Fig. 3 | Stereochemistry & MD analysis of 368. (a) Comparison of the chemical structures and raw sequencing counts in the DEL selections for a series of molecules in the enriched **368** family. *S*-stereoisomers are substantially more enriched than their *R*-counterparts. (b) Chiral chromatography trace demonstrating separation of racemic **368**, conditions which were then used to calculate enantiomeric excess in (*R*)-**368** (c) and (*S*)-**368** (d). Calculated peak parameters for (b-d) are shown below the respective traces. (e) Comparison of the individually synthesized stereoisomers of the racemic **368** “hit”, demonstrating that the *R*-**368** is >100 fold weaker than the *S*-**368** isomer, consistent with the DEL enrichment data. Data are displayed as the average value \pm s.d. with $n = 4$ individual experiments. (f) GTP turnover assay again demonstrating that *S*-**368** retains the ability to potently inhibit fentanyl (5 μ M)-induced GTP turnover like the racemic **368** “hit”, while the *R*-**368** isomer does not display full inhibition even at 20 μ M. Data are displayed as the average \pm s.d. with $n = 6$ individual experiments. (g) Accordingly, the *S*-isomer of **368** was modeled and placed into the cryo-EM density map (blue), along with an

alternate, sub-optimal pose (green) that fits into overlapping but distinct areas in cryoEM density. (h) Both poses were then subjected to MD simulation for three independent 200 ns simulations (without Nb6) (green). An alternate pose from the “opposite” orientation of the NAM in the binding site that (sub-optimally) fits into the cryoEM density was also subjected to three independent 200 ns simulations (blue). The overall root mean square deviations (r.m.s.d.) throughout the trajectory were calculated for protein C α and all atoms in **368** and naloxone for comparison. The time-dependent r.m.s.d. of **368** throughout all trajectories is displayed in (h) and the average of each of the runs with error bars representing the s.d. of three independent simulation averages is displayed in (i). (j) Example simulation snapshots were overlaid by C α alignment for both poses at 4 ns increments. For our chosen pose, the conformation of **368** remains nearly constant throughout all three simulations, with r.m.s.d. values near that for the protein C α (h-j). While C α and naloxone remain stable in both poses (i), the alternate **368** pose is unstable (h-j), resulting in very high r.m.s.d. values and extensive conformational sampling in the orthosteric vestibule region (j).



Extended Data Fig. 4 | Mutational analysis of 368 binding site. (a) Titration of (*S*)-368 against either wild type μOR (red), A323L μOR (purple) or I171W μOR (pink) expressing membranes demonstrates that both mutations substantially inhibit the ability of the NAM to enhance ³H-naloxone affinity. Data are displayed as the average ± s.e.m. with $n = 4$ individual experiments. (b) Expression levels of wild type human μOR (normalized to 100%) compared to mutations used in TRUPATH studies. Data are displayed as the average ± s.e.m. with $n = 9$ individual experiments. (c) Morphine dose-response curves observed by G_i recruitment to human μOR using the TRUPATH assay, again comparing wild type with point mutants. Data are displayed as the average ± s.e.m. with $n = 9$ individual experiments. Dose-response curves in c and d were fit using a three-parameter model for bottom, top, and logEC₅₀ values. Log EC₅₀ values for each curve, along with the 95% confidence interval range, are displayed for all curves.

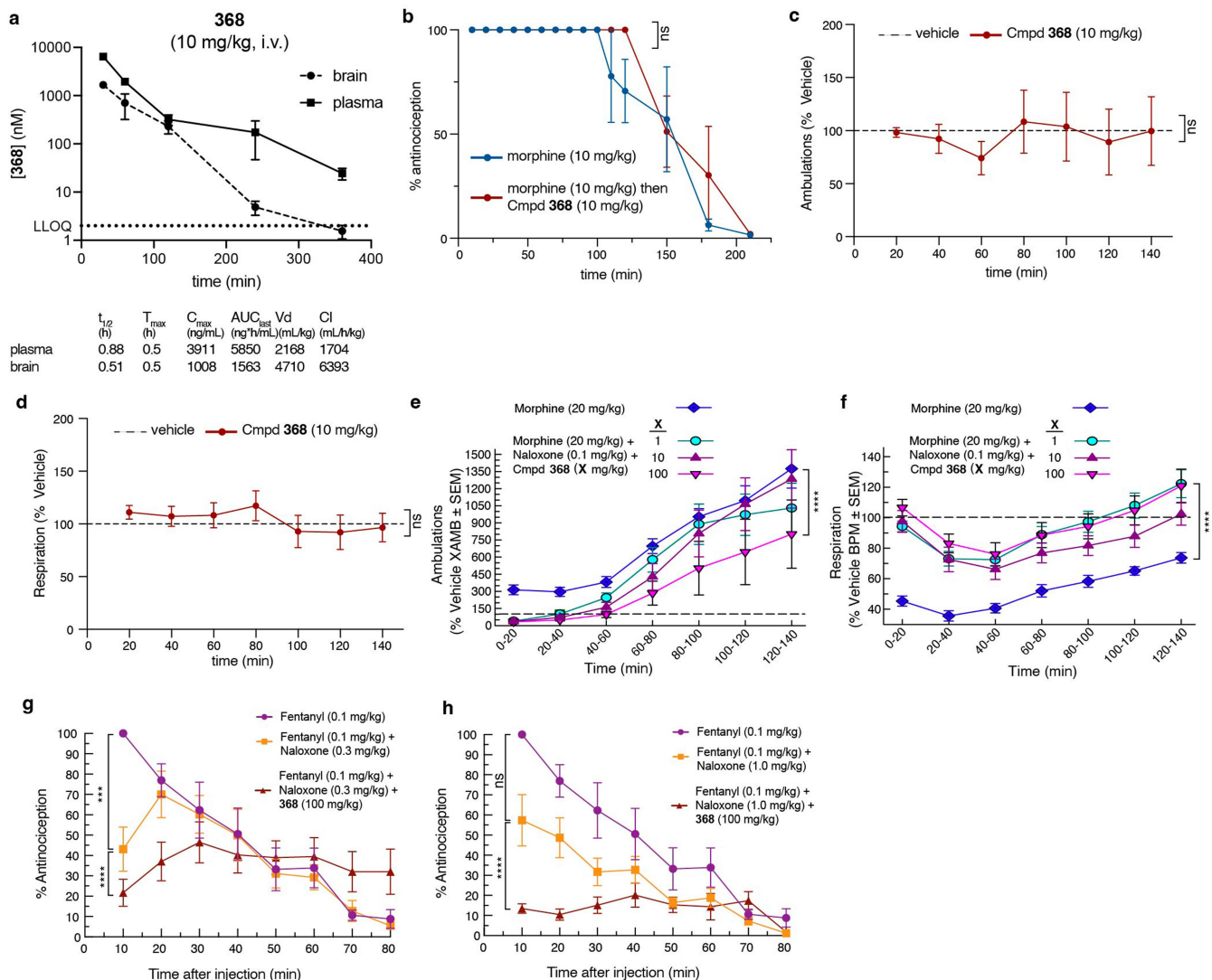
numbers correspond to those in the mouse μOR sequence used for the structural studies. Data are displayed as the average ± s.e.m. with $n = 9$ individual experiments. (d) Fentanyl dose-response curves observed by G_i recruitment to human μOR using the TRUPATH assay, again comparing wild type with point mutants. Data are displayed as the average ± s.e.m. with $n = 9$ individual experiments. Dose-response curves in c and d were fit using a three-parameter model for bottom, top, and logEC₅₀ values. Log EC₅₀ values for each curve, along with the 95% confidence interval range, are displayed for all curves.



Extended Data Fig. 5 | Probe dependence and opioid receptor selectivity of 368. (a) Comparison of the extracellular vestibule regions of the previous β -FNA-bound μ OR and the current naloxone-NAM-bound μ OR. The presence of **368** sterically restricts the ability of small molecule antagonists to enter/exit the orthosteric site. (b) Alignment of the receptor regions of various ligand-bound μ OR structures demonstrate that small molecule orthosteric compounds (top; naloxone [present work], lofentanil [PDB: 7T2H], MP [PDB:7T2G]) have little steric clash with **368** (calculated as the number of atoms in the orthosteric ligand within 1.5 Å of **368**), while both peptide agonists (bottom; β -endorphin [PDB: 8F7Q], DAMGO [PDB: 6DDE]) have clear and substantial steric clash when overlaid with the **368** binding site. (c-e) TRUPATH assays for G_i activation for three different opioid receptor/ligand

pairs; (c) μ OR/DAMGO, (d) δ OR/DPDPE, (e) κ OR/U50488. Data are displayed as the average \pm s.d. with $n = 6$ individual experiments. Fitted agonist EC50 values for each curve are shown, along with the error values which correspond to the 95% confidence interval for the fitted values. **368** has the largest impact on DAMGO activation of μ OR and shows some activity against δ OR activation by DPDPE, but has no effects on κ OR activation by U50488. (f) Sequence alignment of human μ OR, δ OR and κ OR at structural elements with interaction with **368** (residues within 6 Å denoted with an *). Numbering refers to positions within the human μ OR. Red asterisks denote residues with important interactions with **368** but have side chains that are predicted to clash or no longer form productive interactions with **368**.

Article



Extended Data Fig. 6 | In vivo behavior of 368. (a) Pharmacokinetics measurements of 368 at 10 mg/kg administered intravenously. 368 enters the brain with a maximum concentration of 1.66 uM, well above the observed affinity of the compound from radioligand binding (133 nM), but significantly lower than the concentration needed to inhibit agonist activity in cell assays. Data are displayed as the averages \pm s.e.m. with $n = 4$ individuals. (b) In the absence of naloxone, 368 does not have significant effects on morphine-induced antinociception in the 55 °C warm-water tail-withdrawal assay ($F_{(14,84)} = 0.80$, $p = 0.67$; Two-way RM ANOVA; $n = 8$ mice per group). This contrasts to the observed potentiated antagonism when in the presence of a low-dose (0.1 mg/kg) of naloxone (Fig. 4b). (c,d) The CLAMS assay with $n = 8$ mice demonstrates that in the absence of orthosteric compounds, 368 alone (10 mg/kg) has no significant impact on ambulation ($F_{(6,108)} = 0.36$, $p = 0.90$; Two-way RM ANOVA) (c) and respiration ($F_{(6,108)} = 1.19$, $p = 0.32$; Two-way RM ANOVA) (d). (e,f) CLAMS assay with $n = 12$ mice/group ($n = 8$ for morphine alone) demonstrating a dose- and time-dependent ability of 368 to potentiate low-dose (0.1 mg/kg) naloxone in reversing morphine-induced hyperlocomotion ($F_{(24,306)} = 4.27$, $p < 0.0001$; Two-way RM ANOVA; e) and respiratory depression ($F_{(24,294)} = 5.00$, $p < 0.0001$; Two-way RM ANOVA; f), with a maximal effect observed at 100 mg/kg 368 for both. (g) Antinociceptive time course experiment with $n = 8$ mice/group demonstrating that a 0.3 mg/kg dose of naloxone is able to partially reverse fentanyl (0.1 mg/kg)-induced antinociception on its own (factor: dose \times time; Two-way RM ANOVA, $F_{(7,98)} = 3.883$, $p = 0.001$; purple vs. orange curves), addition of 368 results in a significant enhancement of this naloxone-induced reversal (Two-way RM ANOVA, $F_{(7,98)} = 7.069$, $p < 0.0001$; orange vs. dark red curves, $n = 12$ mice). Data for are displayed as the average percent antinociception \pm s.e.m. of $n = 8$ or 12 mice as detailed above. (h) Antinociceptive time course experiment demonstrating that a 1.0 mg/kg dose of naloxone are not significantly able to reverse fentanyl (0.1 mg/kg)-induced antinociception ($F_{(7,98)} = 1.947$, $p = 0.070$; purple vs. orange curves), addition of 368 results in a significant enhancement of this naloxone-induced reversal ($F_{(7,98)} = 7.077$, $p < 0.0001$; orange vs. dark red curves). Data for are displayed as the average percent antinociception \pm s.e.m. of $n = 8$ mice.

Two-way RM ANOVA; e) and respiratory depression ($F_{(24,294)} = 5.00$, $p < 0.0001$; Two-way RM ANOVA; f), with a maximal effect observed at 100 mg/kg 368 for both. (g) Antinociceptive time course experiment with $n = 8$ mice/group demonstrating that a 0.3 mg/kg dose of naloxone is able to partially reverse fentanyl (0.1 mg/kg)-induced antinociception on its own (factor: dose \times time; Two-way RM ANOVA, $F_{(7,98)} = 3.883$, $p = 0.001$; purple vs. orange curves), addition of 368 results in a significant enhancement of this naloxone-induced reversal (Two-way RM ANOVA, $F_{(7,98)} = 7.069$, $p < 0.0001$; orange vs. dark red curves, $n = 12$ mice). Data for are displayed as the average percent antinociception \pm s.e.m. of $n = 8$ or 12 mice as detailed above. (h) Antinociceptive time course experiment demonstrating that a 1.0 mg/kg dose of naloxone are not significantly able to reverse fentanyl (0.1 mg/kg)-induced antinociception ($F_{(7,98)} = 1.947$, $p = 0.070$; purple vs. orange curves), addition of 368 results in a significant enhancement of this naloxone-induced reversal ($F_{(7,98)} = 7.077$, $p < 0.0001$; orange vs. dark red curves). Data for are displayed as the average percent antinociception \pm s.e.m. of $n = 8$ mice.

Extended Data Table 1 | Enrichment properties of selected 368 family members

Compound	Counts C1	Counts C2	Counts C3
368			
10105-368-30-605-0*	595	0	0
10105-390-30-605-0	847	2	0
10105-149-30-605-0	103	1	0
10105-368-30-445-0	80	0	0
10105-368-30-445-0	80	0	0
10105-191-30-605-0	53	0	0

Sequence counts in each of the four selection conditions for family members selected for further study (asterisks identify the exact molecule selected for synthesis and characterization).

For **368**, the second fragment (identifier 30) is rigidly maintained, though other enriched family members also contain the original fragment 1 (identifier 368) or fragment 3 (identifier 605).

C1-C3 correspond to the DEL selection conditions described in Fig. 1. C1 – μ OR/naloxone, C2 – μ OR/met-enkephalin/G_i, C3 – no target control.

Article

Extended Data Table 2 | Summary of TRUPATH potency values for $G_{i/o/z}$ activation

pEC ₅₀ ± SEM, M	368 (μM)	Orthosteric μOR agonists		
		Morphine	Fentanyl	Met-enkephalin
G α i1	0	8.29 ± 0.15	8.57 ± 0.11	8.64 ± 0.10
	90	7.09 ± 0.17	7.31 ± 0.10	7.44 ± 0.14
G α i2	0	8.01 ± 0.22	8.65 ± 0.17	8.61 ± 0.16
	90	6.95 ± 0.26	7.33 ± 0.23	7.26 ± 0.32
G α i3	0	8.06 ± 0.18	8.43 ± 0.15	8.43 ± 0.14
	90	6.72 ± 0.25	7.15 ± 0.12	7.28 ± 0.10
G α oA	0	8.40 ± 0.15	8.83 ± 0.11	8.82 ± 0.10
	90	7.28 ± 0.17	7.71 ± 0.19	7.60 ± 0.22
G α oB	0	8.47 ± 0.11	8.75 ± 0.10	8.89 ± 0.11
	90	7.34 ± 0.21	7.64 ± 0.15	7.75 ± 0.13
G α Z	0	8.56 ± 0.11	8.98 ± 0.10	9.12 ± 0.10
	90	7.48 ± 0.12	7.83 ± 0.14	7.97 ± 0.16

Potency values for three orthosteric μOR agonists (morphine, fentanyl, and met-enkephalin) reported in Extended Data Fig. 1e-g in the absence (0) or presence (90 μM) of **368**. Potency (Log EC₅₀, M) is derived from simultaneous fitting of all biological replicates (n = 3 experiments each done in duplicate). Error values are correspond to the 95% confidence likelihood for the fitted values.

Extended Data Table 3 | Cryo-EM data collection, refinement and validation statistics

368, naloxone, and Nb6-bound μOR- κ _{ICL3} (EMD-44635) (PDB 9BJK)	
Data collection and processing	
Magnification	165000
Voltage (kV)	300
Electron exposure (e ⁻ /Å ²)	60
Defocus range (μm)	0.6-1.4
Pixel size (Å)	0.741
Symmetry imposed	C1
Initial particle images (no.)	4,254,557
Final particle images (no.)	128,613
Map resolution (Å)	3.3
FSC threshold	0.143
Map resolution range (Å)	2.8-3.6
Refinement	
Initial model used (PDB code)	7UL4
Model resolution (Å)	3.7
FSC threshold	0.5
Model resolution range (Å)	18.6-3.7
Map sharpening B factor (Å ²)	-159.9
Model composition	
Non-hydrogen atoms	2525
Protein residues	338
Ligands	2
B factors (Å ²)	
Protein	82.24
Ligand	67.48
R.m.s. deviations	
Bond lengths (Å)	0.014
Bond angles (°)	1.093
Validation	
MolProbity score	1.99
Clashscore	11.27
Poor rotamers (%)	0
Ramachandran plot	
Favored (%)	93.60
Allowed (%)	6.40
Disallowed (%)	0.00

Article

Extended Data Table 4 | Summary of behavioral endpoints of naloxone-precipitated withdrawal in saline-treated or morphine-dependent mice following administration of either vehicle or 368 and naloxone (NAL)

Measure:	Condition 1		Condition 2		Condition 3		Condition 4		ANOVA result:
	saline + NAL	Avg	morphine + NAL	Avg	SEM	morphine + low NAL	Avg	SEM	
Forepaw Tremor	26.7	12.4	26.7	12.4	7.3	2.381	1.6	1.6	$F_{(3,37)}=2.05, p=0.12$
Wet Dog shakes	1	0.33	1.91	0.55	1	0.298	1.1	0.314	$F_{(3,37)}=1.29, p=0.29$
Straightening	0.1	0.1	0.55	0.31	3.1	1.636	0.2	0.133	$F_{(3,37)}=2.95, p=0.05$
Stool Consistency	1.6	0.45	7.46*	1.21	9.3*	0.883	1.3†	0.367	$F_{(3,37)}=23.8, p<0.0001$
Jumping Frequency	2.7	1.92	76.9*	11.9	45.4*†	6.578	32.9*†	4.306	$F_{(3,37)}=17.0, p<0.0001$
Rearing Frequency	23.5	7.54	2.64*	1.25	22.2	3.699	1.6*	0.686	$F_{(3,37)}=8.29, p=0.0002$
Forepaw Licking Frequency	6†	1.97	1.91	1.12	1.8	0.49	0.6	0.499	$F_{(3,37)}=3.88, p=0.02$
Teeth Chattering Frequency	1	1	54.2*	13.2	0.7†	0.3	10.9†	2.858	$F_{(3,37)}=12.8, p<0.0001$

Average and s.e.m. values for $n=10$ mice per group (11 mice for morphine + NAL, condition 2) for 5-day treatment with saline or morphine, followed by naloxone (condition 1 and 2 at 10 mg/kg, or a low dose of 0.1 mg/kg for condition 3 and 4) with or without **368** pretreatment (100 mg/kg, condition 3). One-way ANOVA results included, with Tukey's post-hoc test denoting * $p<0.05$ versus Saline control, † $p<0.05$ versus Morphine + Nal (10 mg/kg) control.

Reporting Summary

Nature Portfolio wishes to improve the reproducibility of the work that we publish. This form provides structure for consistency and transparency in reporting. For further information on Nature Portfolio policies, see our [Editorial Policies](#) and the [Editorial Policy Checklist](#).

Statistics

For all statistical analyses, confirm that the following items are present in the figure legend, table legend, main text, or Methods section.

- | | |
|-------------------------------------|--|
| n/a | Confirmed |
| <input type="checkbox"/> | <input checked="" type="checkbox"/> The exact sample size (n) for each experimental group/condition, given as a discrete number and unit of measurement |
| <input type="checkbox"/> | <input checked="" type="checkbox"/> A statement on whether measurements were taken from distinct samples or whether the same sample was measured repeatedly |
| <input type="checkbox"/> | <input checked="" type="checkbox"/> The statistical test(s) used AND whether they are one- or two-sided
<i>Only common tests should be described solely by name; describe more complex techniques in the Methods section.</i> |
| <input checked="" type="checkbox"/> | <input type="checkbox"/> A description of all covariates tested |
| <input type="checkbox"/> | <input checked="" type="checkbox"/> A description of any assumptions or corrections, such as tests of normality and adjustment for multiple comparisons |
| <input type="checkbox"/> | <input checked="" type="checkbox"/> A full description of the statistical parameters including central tendency (e.g. means) or other basic estimates (e.g. regression coefficient) AND variation (e.g. standard deviation) or associated estimates of uncertainty (e.g. confidence intervals) |
| <input type="checkbox"/> | <input checked="" type="checkbox"/> For null hypothesis testing, the test statistic (e.g. F , t , r) with confidence intervals, effect sizes, degrees of freedom and P value noted
<i>Give P values as exact values whenever suitable.</i> |
| <input checked="" type="checkbox"/> | <input type="checkbox"/> For Bayesian analysis, information on the choice of priors and Markov chain Monte Carlo settings |
| <input checked="" type="checkbox"/> | <input type="checkbox"/> For hierarchical and complex designs, identification of the appropriate level for tests and full reporting of outcomes |
| <input checked="" type="checkbox"/> | <input type="checkbox"/> Estimates of effect sizes (e.g. Cohen's d , Pearson's r), indicating how they were calculated |

Our web collection on [statistics for biologists](#) contains articles on many of the points above.

Software and code

Policy information about [availability of computer code](#)

Data collection EPU 3, CHARMM-GUI, OpenMM 7, Bruker Topspin 3.5 pl 6,

Data analysis GraphPad Prism ver. 9, RELION-3, MotionCor2, CTFFIND4, cryoSPARC v3.3, UCSF Chimera v1.15, COOT 0.8.9.2, phenix-1.19.2, MDAnalysis v2.7.0, PyMOL v2.3.5, UCSF Chimera X v1.1.1,

For manuscripts utilizing custom algorithms or software that are central to the research but not yet described in published literature, software must be made available to editors and reviewers. We strongly encourage code deposition in a community repository (e.g. GitHub). See the Nature Portfolio [guidelines for submitting code & software](#) for further information.

Data

Policy information about [availability of data](#)

All manuscripts must include a [data availability statement](#). This statement should provide the following information, where applicable:

- Accession codes, unique identifiers, or web links for publicly available datasets
- A description of any restrictions on data availability
- For clinical datasets or third party data, please ensure that the statement adheres to our [policy](#)

The authors declare that all data supporting the findings of this study are available within the article, Extended Data, Supplementary Information, or the associated Data Tables. Original raw data will be provided upon request for all experiments, including supporting information. The cryo-EM density map has been deposited in

the Electron Microscopy Data Bank (EMDB) under accession code EMD-44635. Model coordinates have been deposited in the Protein Data Bank (PDB) under accession number 9BJK. Source data are provided with this paper.

Research involving human participants, their data, or biological material

Policy information about studies with [human participants or human data](#). See also policy information about [sex, gender \(identity/presentation\), and sexual orientation](#) and [race, ethnicity and racism](#).

Reporting on sex and gender

N/A

Reporting on race, ethnicity, or other socially relevant groupings

N/A

Population characteristics

N/A

Recruitment

N/A

Ethics oversight

N/A

Note that full information on the approval of the study protocol must also be provided in the manuscript.

Field-specific reporting

Please select the one below that is the best fit for your research. If you are not sure, read the appropriate sections before making your selection.

Life sciences

Behavioural & social sciences

Ecological, evolutionary & environmental sciences

For a reference copy of the document with all sections, see nature.com/documents/nr-reporting-summary-flat.pdf

Life sciences study design

All studies must disclose on these points even when the disclosure is negative.

Sample size

Number of technical replicates and biological replicates are reported in the figure and table legends. Sample size was determined based on variability of the response deviating from the mean as indicated by the standard error of the mean (SEM), which is also represented in the figures. Aiming for 95% power with an alpha significance of p=0.05, and an ANOVA analysis with repeated measures within-between interaction, G*Power 3.19.2 was used to calculate a minimum number of mice per testing condition. Analysis suggests a minimum n of 8 mice per condition will be needed for most antinociception assays, 10 for the tests of physical dependence, 12 for most respiratory/ambulation assays, and 24 for the CPP assays. Sample sizes for all biochemical and cell-based assays were not predetermined and experiments were based on previous experience with particular experimental and sample variability in an effort to be statistically confident in observed changes.

Data exclusions

No data were excluded for this study.

Replication

Data were replicated using technical and independent replicates. See figure and table legends for specific details.

Randomization

Mice were randomly assigned to groups for the behavioral studies. Samples for all other studies were also randomly allocated.

Blinding

The screening of analogs was done by researchers blinded to the identity of the compound. To further confirm efficacy and receptor selectivity we ran blinded experiments. The analgesia experiments done on male C57BL/6J wild-type mice otherwise (24–38 g) were performed by experimenters blinded to the identity of the compound. Blinding experiments for biochemical and structural data were not possible nor necessary as no subjective assessment was required.

Reporting for specific materials, systems and methods

We require information from authors about some types of materials, experimental systems and methods used in many studies. Here, indicate whether each material, system or method listed is relevant to your study. If you are not sure if a list item applies to your research, read the appropriate section before selecting a response.

Materials & experimental systems

n/a	Involved in the study
<input type="checkbox"/>	<input checked="" type="checkbox"/> Antibodies
<input type="checkbox"/>	<input checked="" type="checkbox"/> Eukaryotic cell lines
<input checked="" type="checkbox"/>	<input type="checkbox"/> Palaeontology and archaeology
<input type="checkbox"/>	<input checked="" type="checkbox"/> Animals and other organisms
<input checked="" type="checkbox"/>	<input type="checkbox"/> Clinical data
<input checked="" type="checkbox"/>	<input type="checkbox"/> Dual use research of concern
<input checked="" type="checkbox"/>	<input type="checkbox"/> Plants

Methods

n/a	Involved in the study
	<input type="checkbox"/> <input checked="" type="checkbox"/> ChIP-seq
	<input type="checkbox"/> <input checked="" type="checkbox"/> Flow cytometry
	<input type="checkbox"/> <input checked="" type="checkbox"/> MRI-based neuroimaging

Antibodies

Antibodies used

Monoclonal ANTI-FLAG M2-Peroxidase (HRP) antibody produced in mouse, Sigma-Aldrich, A8592

Validation

Please note manufacturers validation on the product website (<https://www.sigmaaldrich.com/US/en/product/sigma/a8592>) verifying minimum detection amounts and titers for the antibody as well as the associated data sheet.

Eukaryotic cell lines

Policy information about [cell lines and Sex and Gender in Research](#)

Cell line source(s)

Sf9 insect cells (Expression Systems), Cat 94-001S
Tni insect cells (Expression Systems), Cat 94-011S
Expi293F Inducible cells (Thermo Fisher), Cat A39251

Authentication

Cell lines are maintained by supplier. No additional authentication was performed by the study authors.

Mycoplasma contamination

Cell lines are tested by the manufacturers for contamination but were not further tested by study authors.

Commonly misidentified lines (See [ICLAC](#) register)

No commonly misidentified lines were used in this study.

Animals and other research organisms

Policy information about [studies involving animals; ARRIVE guidelines](#) recommended for reporting animal research, and [Sex and Gender in Research](#)

Laboratory animals

Male C57BL/6J mice (24–38 g) were purchased from Jackson Laboratories (Bar Harbor, ME). All mice used throughout the manuscript were opioid naïve. All mice were maintained on a 12 hr light/dark cycle with Purina rodent chow and water available ad libitum, and housed in groups of five until testing. All mice were 8–13 weeks old.

Wild animals

Study did not involve wild animals.

Reporting on sex

Male subjects were used in this initial study to avoid complications arising from the estrous cycle in the responses of female mice.

Field-collected samples

Study did not involve collected samples collected from field.

Ethics oversight

All animals studies were preapproved by the Animal Care and Use committees of the University of Florida in accordance with the 2002 National Institutes of Health Guide for the care and use of laboratory animals.

Note that full information on the approval of the study protocol must also be provided in the manuscript.

Plants

Seed stocks

Report on the source of all seed stocks or other plant material used. If applicable, state the seed stock centre and catalogue number. If plant specimens were collected from the field, describe the collection location, date and sampling procedures.

Novel plant genotypes

Describe the methods by which all novel plant genotypes were produced. This includes those generated by transgenic approaches, gene editing, chemical/radiation-based mutagenesis and hybridization. For transgenic lines, describe the transformation method, the number of independent lines analyzed and the generation upon which experiments were performed. For gene-edited lines, describe the editor used, the endogenous sequence targeted for editing, the targeting guide RNA sequence (if applicable) and how the editor was applied.

Authentication

Describe any authentication procedures for each seed-stock used or novel genotype generated. Describe any experiments used to assess the effect of a mutation and, where applicable, how potential secondary effects (e.g. second site T-DNA insertions, mosaicism, off-target gene editing) were examined.